bioRxiv preprint doi: https://doi.org/10.1101/2023.04.05.535688; this version posted April 11, 2023. The copyright holder for this preprint (which was not certified by peer review) is the author/funder, who has granted bioRxiv a license to display the preprint in perpetuity. It is made available under aCC-BY-NC-ND 4.0 International license.

Calcineurin inhibitor nephrotoxicity revisited: perspectives emerging from differential impact on renal compartments

Hasan Demirci[1,7], Suncica Popovic[1], Carsten Dittmayer[2], Duygu Elif Yilmaz[1], Ismail Amr El-Shimy[3], Michael Mülleder[4], Christian Hinze[5], Kerim Mutig[1,6], Sebastian Bachmann[1,7]

[1]Institute of Functional Anatomy, Charité - Universitätsmedizin Berlin, Berlin, Germany

[2]Department of Neuropathology, Charité - Universitätsmedizin Berlin, Berlin, Germany

[3]Molecular Epidemiology Unit, Berlin Institute of Health, Charité - Universitätsmedizin Berlin, Berlin, Germany

[4]Core Facility-High-Throughput Mass Spectrometry, Charité - Universitätsmedizin Berlin, Berlin Germany

[5]Department of Nephrology and Hypertension, Hannover Medical School, Hannover, Germany

[6]Department of Translational Physiology, Charité - Universitätsmedizin Berlin, Berlin, Germany.

[7]Department of Cell- and Neurobiology, Charité - Universitätsmedizin Berlin, Berlin Germany

Corresponding author: Sebastian Bachmann, Prof. Dr.

Charité - Universitätsmedizin Berlin

Campus Mitte

Institut für Zell- und Neurobiologie

Charitéplatz 1

10117 Berlin, Germany

Tel.: +49 30 450 528 001

Fax: + 49 30 450 528 922

E-mail: sbachm@charite.de

bioRxiv preprint doi: https://doi.org/10.1101/2023.04.05.535688; this version posted April 11, 2023. The copyright holder for this preprint (which was not certified by peer review) is the author/funder, who has granted bioRxiv a license to display the preprint in perpetuity. It is made available under aCC-BY-NC-ND 4.0 International license.

Conflict of interest: The authors have declared that no conflict of interest exists.

Keywords: Cyclosporine A, Tacrolimus, CNI nephropathy, Pore endothelium, VEGF, Proximal tubule, Unfolded protein response, Multiomics

bioRxiv preprint doi: https://doi.org/10.1101/2023.04.05.535688; this version posted April 11, 2023. The copyright holder for this preprint (which was not certified by peer review) is the author/funder, who has granted bioRxiv a license to display the preprint in perpetuity. It is made available under aCC-BY-NC-ND 4.0 International license.

Abstract

Calcineurin inhibitors (CNI) are the backbone for immunosuppression after solid organ transplantation. Although successful in preventing kidney transplant rejection, their nephrotoxic side effects notoriously contribute to allograft injury despite attempts to optimize their application, often with additional medications. The etiology of chronic renal parenchymal changes is complex irrespective of chosen therapy with either cyclosporine A (CsA) or currently favoured tacrolimus (Tac). The pathogenetic detail of their respective toxicities has not been fully understood. To test whether CsA and Tac cause adverse renal responses differentially, we employed a chronic rat model with continous drug application. Histopathology of the renal compartments was combined with multiomics analysis. Both drugs caused significant albeit differential damage in vasculature and nephron. The glomerular filtration barrier was more affected by Tac than by CsA, showing prominent deteriorations in pore endothelium and podocytes along with impaired VEGF/VEGFR2 signaling and podocyte-specific gene expression. By contrast, proximal tubule epithelia were more severely affected by CsA than by Tac, revealing lysosomal dysfunction and enhanced apoptosis along with impaired proteostasis and oxidative stress. We conclude that pathogenetic alterations in renal microenvironments are specific for either treatment. We have identified related biomarkers to adequately address chronic CNI nephropathy in transplant recipients.

bioRxiv preprint doi: https://doi.org/10.1101/2023.04.05.535688; this version posted April 11, 2023. The copyright holder for this preprint (which was not certified by peer review) is the author/funder, who has granted bioRxiv a license to display the preprint in perpetuity. It is made available under aCC-BY-NC-ND 4.0 International license.

Introduction

Calcineurin inhibitors (CNI) such as cyclosporine A (CsA) and tacrolimus (Tac, FK506) have become the basis for immunosuppressive treatment in organ transplant recipients and patients with autoimmune diseases over the past four decades. Today, over 90% of kidney transplant recipients in Western countries are maintained on CNI-containing immunosuppressive regimens. In spite of a satisfactory outcome at short term, chronic use of CNI causes nephrotoxicity (NTX) in a significant proportion of renal and nonrenal transplant recipients, affecting renal allograft function (1–3). Minimizing CNI dosage, sometimes aided with mycophenolate and/or corticosteroids, has mitigated damage in many cases but is complicated by the difficult assessment for clinical signs of under-immunosuppression. Switching between CNIs, CNI elimination, or substituting with other immunosuppressant regimens have been explored as well, but to date, alternatives to CNIs are widely considered unequal (1,4,5). In CNI-NTX, progressive decline in allograft function is currently regarded to root from a combination of chronic hypoperfusion related with hyaline arteriolopathy and glomerular scarring, and direct tubular toxicity causing vacuolation, atrophy, and striped fibrosis which together have been termed interstitial fibrosis/tubular atrophy (IF/TA; 2,6,7). Specificity of these pathological landmarks has been questioned repeatedly for similarities to immunological damage and other comorbidities mostly unrelated with CNI (7,8). A large body of human data and results from cell and animal studies have grown over time to clarify this issue.

CNI address ubiquitously expressed calcineurin, a calcium/calmodulin-dependent serine-threonine phosphatase, notable for its key role in T cell function. Upon activation, the catalytic subunit of calcineurin (CnA) associates with the regulatory subunit (CnB) to dephosphorylate and thereby activate transcription factors of the NFAT (nuclear factor of activated T-cells) family to induce expression of key genes for T-lymphocyte differentiation (9,10). Calcineurin and NFAT isoforms are, however, not T-cell specific and may encompass interactions with other substrates, targeting proteins and regulators of calcineurin activity beyond immunology. CNI nephrotoxicity has thus been functionally referred to salt-sensitive

bioRxiv preprint doi: https://doi.org/10.1101/2023.04.05.535688; this version posted April 11, 2023. The copyright holder for this preprint (which was not certified by peer review) is the author/funder, who has granted bioRxiv a license to display the preprint in perpetuity. It is made available under aCC-BY-NC-ND 4.0 International license.

hypertension, tissue hypoxia, oxidative stress via NADPH oxidase, anemia, hyperkalemia, calcium and magnesium wasting, metabolic acidosis, dysregulation of major endo- and paracrine systems, and metabolic stress (11–17). Vasoconstrictors such as endothelin, arachidonic acid metabolites, and activated renin-angiotensin-aldosterone system (RAAS) components along with exaggerated recruitment of renin-producing cells contribute to vascular dysfunction (2,14). Although it has been stated that CsA and Tac produce identical lesions (7), this has not remained unopposed. Several patient studies and a recent experimental study in cultured human cells suggested that CsA was associated with stronger nephrotoxicity than Tac (3,18,19). Both CNI inhibit calcineurin activity by forming complexes with distinct members of the immunophilin family, i.e. cyclophilins for CsA and FKBP12 for Tac. These distinct interactions served to explain some of the individual toxicity profiles of CsA vs. Tac. Distinctively, CsA affects proteostasis, since the chaperone activity of cyclophilins interacts with protein maturation (20). Studies comparing CsA vs. Tac in cell culture consequently showed stronger association of CsA with ER stress and the unfolded protein response (UPR), leading to accumulation of misfolded protein and apoptotic cell death, whereas Tac did not (18,21–23). CsA-NTX has further been associated with altered JAK/STAT signaling and salt-sensitive mitochondrial dysfunction (24). Transcription factor EB (TFEB)-mediated autophagy flux and lysosomal dysfunction owing to CsA-induced mTOR overactivity have further been addressed in search of potential nephroprotection (25). Regarding the undiminished need for CNI and the current preference to treat transplant recipients with Tac rather than CsA (3) except for new onset of diabetes cases (1) and specific combination therapies, there is an overt need to improve the knowledge of cellular mechanisms of NTX in both settings towards adapting treatment protocols to manage CNI adverse effects for better patient outcomes.

Our central hypothesis was therefore that chronic CsA and Tac regimens, before reaching irreversible damage, affect renal compartments differently, based on distinct pathogenic pathways involved. Previous rodent model studies were often inconclusive due to inconsistency of drug dosage, application time and mode, and combination with salt

bioRxiv preprint doi: https://doi.org/10.1101/2023.04.05.535688; this version posted April 11, 2023. The copyright holder for this preprint (which was not certified by peer review) is the author/funder, who has granted bioRxiv a license to display the preprint in perpetuity. It is made available under aCC-BY-NC-ND 4.0 International license.

deprivation exacerbating vascular pathology. In our study, we have used minipumps for safe and steady drug application in rats, analyzed pathology with state-of-the-art technology, and evaluated multiomics-derived signatures to differentially illustrate cellular mechanisms. Our results identify distinctive mechanisms and related biomarkers in Tac vs. CsA groups serving to link individual pathways to nephroprotective modifications in patient immunosuppressive protocols.

bioRxiv preprint doi: https://doi.org/10.1101/2023.04.05.535688; this version posted April 11, 2023. The copyright holder for this preprint (which was not certified by peer review) is the author/funder, who has granted bioRxiv a license to display the preprint in perpetuity. It is made available under aCC-BY-NC-ND 4.0 International license.

Results

Physiologic Parameters

After 4 weeks of treatment with CNI delivered by osmotic minipumps, mean whole blood trough levels were in agreement with published data in rodents (3.04 µg/mL in the CsA and 3.42 ng/mL in the Tac groups; Table 1; 26,27). CNI-induced kidney injury was assessed in both groups by reduced creatinine clearance, elevated blood urea nitrogen (BUN) and cystatin C levels, and reduced fractional Na^+ excretion. Substantial phosphaturia and glucosuria were found in both groups, whereas albuminuria was elevated only in the CsA group (Fig. 1; for details, see Table 1).

Overview Pathology

Renal structural and gene expressional parameters of the vehicle groups were normal according to established standards. Comparing these with the recipients of CNI, significant pathological changes were registered in the respective perfusion-fixed rat kidney tissues. As envisaged, changes typically ranged between mild onset stages and nephron destruction, modeling progression of CNI-NTX. Mild-to-severe glomerular and tubulo-interstitial degenerative alterations were observed in numerous scattered, circumscribed foci of the cortex, while other areas appeared normal as viewed by periodic acid-Schiff (PAS) staining (Fig. 2A-C). These foci were frequent in the subcapsular cortex but also extending to deeper parts of cortex and outer medulla, initiating striped fibrosis; typically, they consisted of 5 to 20 tubular profiles, but also larger areas measuring up to 150.000 μm^2 were encountered. Numerical evaluation indicated similar incidence and dimension of foci among groups (Fig. 2D). Adjacent glomeruli often displayed a retracted, albeit fully perfused phenotype. Interstitium of the foci was loose and meshwork-like in CsA, but dense and cell-enriched in Tac; in both, standard histology indicated graded fibrosis in the foci by Trichrome and Sirius red staining, and associated basement membranes were thickened in PAS staining (Fig. 2E-K)**.** Local α-SMA-immunoreactive signal suggested intensive profibrotic myofibroblast transdifferentiation and pericyte activation. α-SMA signal was pronounced near atrophic or necrotic tubules and adjacent glomeruli; these showed pericapsular signal to varying extent

bioRxiv preprint doi: https://doi.org/10.1101/2023.04.05.535688; this version posted April 11, 2023. The copyright holder for this preprint (which was not certified by peer review) is the author/funder, who has granted bioRxiv a license to display the preprint in perpetuity. It is made available under aCC-BY-NC-ND 4.0 International license.

with stronger signals encountered in the CsA than in the Tac group (Suppl. Fig. S1A-D). Outer medullary interstitial α-SMA signal was focally enhanced to equal extent in Tac and CsA (Suppl. Fig. S1E-G). In the inner medulla, changes in α-SMA were minimal. Typical cellular infiltrates were scarce, since anti-CD45 immunofluorescence indicated only mild infiltration in fibrotic foci of CsA and Tac samples (Suppl. Fig. S1H-K).

Renal Vasculature

Interlobular arteries, commonly revealing 2 to 3 layers of media cells and modest adventitial collagen, showed mild increases in wall thickness upon CNI with occasional hyalinic or necrotizing subintimal or media inclusions in CsA as opposed to significant increases in intermyocyte matrix and adventitial collagen as well as myocyte thinning in Tac (Suppl. Fig. S2A-D). Glomerular afferent arterioles showed moderate thickening of media and endothelium in CNI with occasional PAS-positive wall inclusions in CsA and increased wall-to-lumen ratio in Tac (Fig. 3A-D). Endothelial CD31 (PECAM-1) expression showed mildly increased signal in CsA and Tac (Fig. 3E-G). Ultrastructurally, myocytes were particularly rich in contractile apparatus of single-layered media in CsA, but flattened and layered in Tac (Fig. 3H-K). Luminal occlusion was not observed. Terminal afferent arterioles regularly displayed hypergranularity of the juxtaglomerular granular cells with both treatments, with renin signal intensities increased 7-fold in CsA and 8.8-fold in Tac compared to controls (Suppl. Fig. 3A-E). Specifically in the Tac group layers of granular cells featured narrowing of the afferent arteriole focally at the glomerular entry (Suppl. Fig. 3D). Transmission electron microscopy (TEM) detail of granular cells was inconspicous in CsA but showed anastomosing multiform granules surrounded by dense accumulations of glycogen in Tac (Suppl. Fig. 3F-G); granular cells focally showed necrosis or hyaline formations (Suppl. Fig. 3H). Interlobular veins and ascending vasa recta viewed by scanning electron microscopy (SEM) were normal in CsA but strikingly revealed partial or total loss of fenestrae in Tac. Focally adhering CD45-positive leukocytes were seen in both CNI groups, but more frequently in Tac (Suppl. Fig. 4).

Glomeruli

bioRxiv preprint doi: https://doi.org/10.1101/2023.04.05.535688; this version posted April 11, 2023. The copyright holder for this preprint (which was not certified by peer review) is the author/funder, who has granted bioRxiv a license to display the preprint in perpetuity. It is made available under aCC-BY-NC-ND 4.0 International license.

Glomeruli of the CNI groups showed normal structure and free capillaries in unaffected areas, wheres stages of mild sclerosis and/or retraction were found in association with fibrotic foci. Here, the tuft sizes were reduced by 18% in CsA and by 14% in Tac, capillaries narrowed, and the mesangium mildly expanded (Fig. 4A-F). Ultrastructure of the capsule revealed an activated, thickened parietal epithelium (from 0.2 up to 4 µm cell height) with occasional vacuolization, layering of the basement membrane and adjacent hyaline or granular matrix formations (Suppl. Fig. 5A,B). Multiple synechiae with podocytes were commonly observed in CsA (Suppl. Fig. 5C-E); changes in Tac were comparable (Suppl. Fig. 5F). Specifying its activated state, CD44 immunostaining showed a sharp increase in parietal epithelial signal in CsA and Tac, and the pericapsular interstitium was mildly (CsA) or substantially (Tac) infiltrated by CD45-positive leukocytes (Suppl. Fig. 5G). Degenerative changes of the glomerular tuft varied with the degree of retraction and podocyte effacement. The glomerular basement membrane (GBM) was often wrinkled along the mesangial stalks in both groups. By SEM, partial podocyte effacement was commonly found in CsA, whereas in Tac, more extensive or generalized effacement with major podocyte degeneration was detected (Fig. 4G-M). Filtration slit density (FSD) was determined confocally by three-dimensional-structured illumination microscopy (3D-SIM) and Podocyte Exact Morphology Measurement Procedure (PEMP) using anti-podocin antibody to label the filtration slit and anti-integrin α3-antibody to visualize underlying GBM. Besides areas of normal configuration of the slit diaphragm, sites of significant effacement were detected in both groups (Fig. 5A-C). Significant FSD reduction was found in both CNI groups with values numerically higher, though more variable in Tac than in CsA (Fig. 5D). These findings were further illustrated by TEM confirming focal effacement, substantially more so in Tac than in CsA (Fig 5 E-G). Endothelial fenestration of the glomerular capillaries showed conspicous reductions in pore density by SEM, again markedly stronger in Tac than in CsA (Fig. 6A-D). In TEM, these changes were confirmed and accompanied by substantial condensation of endothelial cells chiefly in Tac (Fig. 6E-K). Areas of reduced pore formation were commonly facing those of podocyte effacement. The significant reductions in pore density were numerically confirmed

bioRxiv preprint doi: https://doi.org/10.1101/2023.04.05.535688; this version posted April 11, 2023. The copyright holder for this preprint (which was not certified by peer review) is the author/funder, who has granted bioRxiv a license to display the preprint in perpetuity. It is made available under aCC-BY-NC-ND 4.0 International license.

(Fig. 6L). Changes of the tuft structures were paralleled by diminished Wilms' tumor 1 (WT1) particularly in the Tac, but substantially less so in the CsA group (Fig. 7A-C). In turn, cell death-associated DNA fragmentation indicated by TUNEL immunofluorescence of the tuft was highly increased in the Tac, but less so in the CsA group; contrastingly, parietal epithelial cells showed a stronger signal in CsA than in Tac (Fig. 7D-F). These observations were confirmed by numerical quantification (Fig. 7G-J).

Proximal tubule – Initial Changes

The proximal convoluted tubule (PCT; S1 and S2 segments) revealed well-preserved standard morphology in Richardson's blue-stained Veh samples, with pronounced brush border membrane (BBM), apical endosomal apparatus, and 3 to 15 dark-blue stained lysosomes per sectioned cell (Fig. 8A). A variety of early changes were registered upon CNI administration. In CsA, the dark-stained lysosomes were largely absent from PCT but instead, one to several large heteromorphic vacuoles as well as autofluorescent residual bodies were commonly detected per cell. The vacuoles reached nuclear size or beyond and were filled with proteinaceous, PAS-positive content. In Tac, PCT showed less dark-stained lysosomes than in Veh, but only few heteromorphic vacuoles; lysosomal changes were quantified (Fig. 8B). By TEM, PCT apical vesicular compartment, endosomes, fields of dense apical tubules (DAT), and autophagic vesicles with membraneous content, anastomosing with buds of DAT, were normally developed in Veh (Fig. 8C). In CsA, the heteromorphic vacuoles were membrane-bound, showing focally open communication with the cytosol via interrupted membranes as well as anastomoses with other lysosomes, residual bodies with granular content, and late endosomes. Stages of lysosomal exocytosis were frequent (Suppl. Fig. 6A-D). This was confirmed by SEM, showing the highest numbers of cast-like remainders of lysosomal exocytosis within the BBM of CsA samples (Suppl. Fig. 6E-H). The lysosomal nature of the heteromorphic vacuoles was identified by lysosomal associated membrane protein 1 (LAMP1) immunoreactivity forming a luminescent ring along each late endosomal/lysosomal perimeter in the CNI groups. In CsA, LAMP1 luminescent lining was encountered also in exocytotic states of heterolysosome extrusion (Fig. 8D). Abundance of

bioRxiv preprint doi: https://doi.org/10.1101/2023.04.05.535688; this version posted April 11, 2023. The copyright holder for this preprint (which was not certified by peer review) is the author/funder, who has granted bioRxiv a license to display the preprint in perpetuity. It is made available under aCC-BY-NC-ND 4.0 International license.

catalase as an indicator of defense against oxidative stress was elevated in CsA compared to Veh, whereas in Tac there was no difference; these changes were quantified (Suppl. Fig. 7A-D, J). Ultrastructure of peroxisomes was not fundamentally different among groups in TEM, but major clusters of peroxisomes located in basal cell areas were observed (Suppl. Fig. 7E-H). TUNEL immunofluorescence showed clear maxima of nuclear signals in PCT and proximal straight tubule (PST) in CsA as opposed to few scattered signals registered in Tac; Veh control samples were unreactive (Fig. 9A-F). This was confirmed by numerical quantification (Fig. 9G-J).

Proximal Tubule – Progression to Necrosis

Significant degenerative changes were observed in PCT, whereas other nephron segments were less affected. Beyond development of the large heteromorphic cell inclusions, PCT of the CsA group initially showed loss of BBM, transitory increases in DAT and polysomes, and focally thickened basement membrane in TEM. Advanced stages showed flattened epithelia with subtotal or total loss of BBM, assumption of a polygonal cell shape, accumulation of residual bodies and basally located liposomes, stages of mitophagy, loss of peroxisomes, whole cell autophagy. Cystic dilatations occurred focally. In final stages, necrotic epithelia were collapsed and groups of tubules wrapped in a wrinkled matrix coat for future removal (Suppl. Fig. 8A-D). These changes were partly similar in Tac; however, cellular accumulation of residual bodies was not observed, whereas liposomes and mitophagic clusters were more abundant. PCT cells often assumed a polygonal form along with advanced dedifferentiation (Suppl. Fig. 8E-G). Kidney injury molecule-1 (KIM-1), an established marker for proximal tubular injury, showed focal areas of intensive immunoreactive signal in both CNI groups, whereas other nephron portions were unaffected. At low magnification, signals were detected as stripes extending across cortex and outer stripe or as scattered single nephron portions; numerically, signal frequency was similar in CsA and Tac (Suppl. Fig. 9A-D). In more detail, co-staining for KIM-1 and aquaporin-1 (AQP1) revealed that in both groups, onset stages co-expressed both signals in PCT and PST, whereas with advanced necrosis, AQP1 was entirely replaced by KIM-1 signals (Suppl. Fig. 9E-H).

bioRxiv preprint doi: https://doi.org/10.1101/2023.04.05.535688; this version posted April 11, 2023. The copyright holder for this preprint (which was not certified by peer review) is the author/funder, who has granted bioRxiv a license to display the preprint in perpetuity. It is made available under aCC-BY-NC-ND 4.0 International license.

Changes in Cortical Interstitial Vasculature

CD31 immunofluorescence showed strong endothelial signal in the capillary network of the cortical interstitium in Veh (Fig. 10A). Intact tissue areas of the CsA and Tac groups showed undiminished capillary signal, whereas in fibrotic foci, numerous, strongly CD31-positive capillaries of a rounded, sprouting type are detected (Fig. 10B,C). Increases of CD31 abundance were confirmed by Western blot (WB) analysis (Fig. 10D). Changes in endothelial fenestration were quantified from TEM sections; CNI diminished the pore density significantly with a minor decrease in CsA but major in Tac (Fig. 10E-H).

Medullary Changes

In CsA and Tac, outer medullary interstitium was focally widened, showing tubular profiles of irregular or collapsed shape (Suppl. Fig. 10A-C). In these areas, thick ascending limb (TAL) structure was altered in CsA revealing simplified epithelium with loss of membrane folding and mitochondria; surrounding vasculature was rounded and showed thickened endothelium. Comparingly, in Tac the TAL epithelium was similarly simplified, revealing enhanced membrane contrast and basal myelin figures; there were significant glycogen accumulations (Suppl. Fig. 10D-G). Changes in the collecting ducts were minor in both groups; necrotic profiles were encountered occasionally.

Multiomics Analyses

RNA-seq transcriptomic, global proteomic, and phosphoproteomic analyses served to obtain mechanistic perspectives underlying CNI-induced pathology. RNA-seq revealed 1003 differentially expressed genes (DEG; 507 up- and 496 downregulated) in CsA and 323 (105 up- and 218 downregulated) in Tac. Few products were jointly altered, among them increased renin and decreased calbindin excelled (adjusted $P<0.1$; see Venn diagram in Suppl. Fig. 11A; cf. complete list of DEG, Suppl. Table 2A,B). Pathway enrichment analysis of CNI-induced DEGs by Enrichr indicated that among others, *vasculature development*, *glomerular visceral epithelial cell differentiation, actin cytoskeleton organization*, *eukaryotic translation termination*, and *apoptotic process* were upregulated, whereas *proximal tubule transport* and likely associated metabolism were downregulated, supporting CsA-typical

bioRxiv preprint doi: https://doi.org/10.1101/2023.04.05.535688; this version posted April 11, 2023. The copyright holder for this preprint (which was not certified by peer review) is the author/funder, who has granted bioRxiv a license to display the preprint in perpetuity. It is made available under aCC-BY-NC-ND 4.0 International license.

damages. In Tac, *renin-angiotensin system*, *biological oxidations*, *oxidative stress-induced senescence*, *blood vessel endothelial cell proliferation involved in sprouting angiogenesis*, and *vascular wound healing* were up-, and *vasculature development*, *positive regulation of endothelial cell proliferation*, *mTORC1 signaling*, *AMPK signaling pathway*, and *actin filament organization* downregulated, which agreed with Tac-typical structural alterations (Figure 11). Both proteomic and phosphoproteomic data were consistent with these pathways and further selectively pointed to markedly upregulated *unfolded protein response* pathway in CsA but not in Tac; the respective products were verified by WB (Suppl. Fig. 12-14; cf. complete list of differentially expressed proteins (DEP) and phosphoproteins (DEPP), Suppl. Table 2C-F). Among single, differentially regulated products, PDIA5 and phosphorylated PERK (*Eif2ak3*), related with UPR, as well as HMGB1 and CTSD, both regulatory in autophagy, were upregulated in CsA (Suppl. Table 2A,C, E). In Tac, *Prkce, Prkd1, Ptger4*, and *Cav1* transcripts, CAV1 and DDAH2 proteins, and phosphorylated PRKD1, all involved in endothelial function and vasculature changes, were downregulated. Likewise, SYNPO transcript and protein, PALLD transcript and phosphorylation, PODXL protein, and CD2AP phosphorylation, all relevant in podocyte biology, were decreased (Suppl. Table 2B, D, F). We furthermore used the published list of 193 proximal tubule-specific genes identified in rat kidney to compare with the present changes (28). Here, 100 differentially regulated genes (20 up- and 80 downregulated) were altered in CsA, but only 33 genes (25 up- and 8 downregulated) in Tac, confirming the more substantial PT changes in CsA compared to Tac (Suppl. Figure 15).

bioRxiv preprint doi: https://doi.org/10.1101/2023.04.05.535688; this version posted April 11, 2023. The copyright holder for this preprint (which was not certified by peer review) is the author/funder, who has granted bioRxiv a license to display the preprint in perpetuity. It is made available under aCC-BY-NC-ND 4.0 International license.

Discussion

In this experimental study we employed an integrative approach to identify potential mechanisms of CNI nephropathy under early chronic conditions, focussing on its distinctive pathogenesis under CsA vs. Tac medications. State-of-the-art methods, including high-resolution histopathology, candidate RNA and protein assessments as well as comprehensive multiomics allowed us to assign renal microenvironmental remodeling to novel, specific protein signatures. Responses to treatments were distinctive, and potential biomarkers related with both drugs were identified.

Confined foci with partly retracted glomeruli, atrophic tubules, mild fibrosis with α-SMA induction, and moderate inflammation qualified this approach to study CNI nephropathy at its subclinical beginning, before advanced pathology could mask essential regulatory or phenotypic changes characterizing microenvironmental remodeling (1–3,29,30). Overall renal function was shown to be affected by reduced creatinine clearance.

Pathology pointed to distinct onset changes in arteriolar wall changes of the two groups. RAAS stimulation, higher in Tac than in CsA, may have been involved. RhoA-mediated Ang II hypersensitivity of the afferent arteriole along with decreased glomerular filtration rate (GFR) and enhanced generation of reactive oxygen species (ROS) has been found earlier in Tac (31). Disproportionate impairment of vasodilatory prostaglandins in Tac agreed with downregulated of Ep4 receptor (*Ptger4*) and related PGE2 action; this also implied a negative effect on eNOS function (32,33). *Prkce* mRNA, selectively downregulated in Tac, indicated impaired VEGF signaling, since its knockdown in bovine endothelial cells abrogated VEGF-stimulated AKT phosporylation, decreased action of its cognate receptor VEGFR2, and impaired VEGF-stimulated NOS activity (34). Likewise, CAV1 mRNA & protein were downregulated in Tac but not in CsA, supporting related NO deficiency downstream of impaired VEGF signaling (35). Selective upregulation of DDAH2, which degrades endogenous NOS inhibitors such as asymmetric dimethylarginine (ADMA) and monomethyl arginine (L-NMMA), indicated potential compensation to preserve NO availability in Tac (36). Increased leukocyte adhesion, more in Tac than in CsA, pointed to affection of the

bioRxiv preprint doi: https://doi.org/10.1101/2023.04.05.535688; this version posted April 11, 2023. The copyright holder for this preprint (which was not certified by peer review) is the author/funder, who has granted bioRxiv a license to display the preprint in perpetuity. It is made available under aCC-BY-NC-ND 4.0 International license.

endothelial surface and agreed with focal incidence of CD45-positive cell accumulations (37). This difference was possibly related with CsA's beneficial effects on adhesion molecules observed in an *in vitro* context (38). Stimulated endothelial CD31 in both conditions suggested a cytoprotective reaction to altered shear stress (39,40) and/or adjustment for leukocyte transmigration (41).

Fibrotic alterations of Bowman's capsule were prominent in early and advanced glomerular affection both in CsA and Tac. Pronounced CD44 expression, as found in the activated parietal epithelium, has recently been termed a useful marker for early CsA-NTX in human grafts (42). CD45-positive cell accumulations. In conjunction with fibrous podocyte synechiae and CD45-positive cell accumulations these features suggested early stages of sclerotic lesions and onset of inflammation (43,44). Tuft retraction, likely resulting from diminished microvascular perfusion (45), and decreased FSD occurred to similar extent in CsA and Tac, whereas reduced endothelial fenestration was found more in Tac than in CsA. Early work has reported loss of pore density and fenestral size also in a CsA rat model (46). VEGF signaling seems to be centrally involved, since its effects on pore density were reported in conjunction with TNFα signaling in mice (47), and a human microvascular model displayed reduced fenestration and VEGF signaling along with stimulated *Adamts1* and cytoplasmic deteriorations upon CsA (48). Exacerbated condensation of the endothelial cytoplasm was also evident in our Tac samples, and *Adamts1,* along with the transcription factor *Sox17,* was stimulated. *Sox17* status differed in both drugs and may have provided compensatory endothelial repair in CsA, but failed to do so in Tac (49). With caveolin-1 (*Cav1*) substantially diminished at the mRNA and protein level in Tac, our multiomics data further reflected an important link to reduced angiogenesis and pore formation (50,51). This was supported by protein kinase D1 (PRKD1) mRNA and phosporylation selectively downregulated in Tac; PRKD1 also controls VEGFR2, eventually via desinhibition of the transciption factor AP2 (52). Extensive foot process effacement in Tac, more than in CsA, pointed to a distinctively impaired filtration barrier and hydraulic conductivity since indeed, capillary segments with advanced pore rarefaction showed parallel podocyte effacement. This agreed with

bioRxiv preprint doi: https://doi.org/10.1101/2023.04.05.535688; this version posted April 11, 2023. The copyright holder for this preprint (which was not certified by peer review) is the author/funder, who has granted bioRxiv a license to display the preprint in perpetuity. It is made available under aCC-BY-NC-ND 4.0 International license.

decreased WT1 and increased TUNEL signals in podocytes, both exacerbated in Tac. In fact, diminution of WT1, an established marker of podocytes, has been associated with loss of prominent barrier functions (53) and early changes towards glomerulosclerosis (54), while enhanced TUNEL signals stood for apoptosis or repair stages (55). Key podocyte genes such as palladin, CD2AP, synaptopodin, nephronectin, and podocalyxin, all intrinsic structural components of podocytes, were selectively downregulated in Tac which also underscores higher podocyte damage compared to CsA, and concomitant impairment in shape and motility of their foot processes (56,57). Associated decrease in phosphorylation of CD2AP, a stabilizing protein of the slit diaphragm, at Ser 404 may reflect further loss of function (58). Although in their longitudinal histological cohort study, Nankivell and colleagues reported equal glomerular damage scores in CsA and Tac samples (3), our results thus suggest a selectively higher burden on glomeruli in the Tac group at an early stage.

Tubular damage in CNI nephropathy has been extensively discussed in the past, yet it has remained uncertain whether direct toxicity to epithelia or downstream effects of affected vasculature or glomerular function prevail at its origin. Published data point to the proximal tubule as the principal nephron segment involved in pathogenesis, reporting vacuolization, loss of BBM, bioenergetic maladaptation, atrophy, and fibrotic decay with no major causative distinction between CsA and Tac (59,60). Contrastingly, our data have shown substantial differences in proximal tubular damage. The known isometric vacuolization, believed to be reversible, originates from ER dilatations in acute settings and does not apply here. Our major finding was the massive accumulation of heterolysosomes, identifed by their LAMP1-positive boundaries, and their exocytotic luminal extrusion predominantly in the CsA group, whereas changes in Tac were much less lysosomal-based. Our multiomics data confirmed milder tubulotoxicity with Tac which harmonized with the current trend of its preferential use in organ transplantation (1,3). The highly significant rise in activated PERK as a critical regulator and essential component of the UPR as well as the stimulated products IRE1, another principal UPR transducer, and downstream spliced XBP1 (sXBP1) underlined the

bioRxiv preprint doi: https://doi.org/10.1101/2023.04.05.535688; this version posted April 11, 2023. The copyright holder for this preprint (which was not certified by peer review) is the author/funder, who has granted bioRxiv a license to display the preprint in perpetuity. It is made available under aCC-BY-NC-ND 4.0 International license.

canonical cascades which, under the given chronic conditions, likely caused the rise in cleaved caspase-3 (c-casp3) and related apoptosis shown here in CsA but not in Tac (21,61,62). In line with this, we and others have previously noticed impaired proteostasis and UPR leading to proapoptotic ER stress upon CsA but not Tac at short term (18,23). We also found PDIA5, a disulfide isomerase required for ATF6 activation, upregulated suggesting involvement of the third UPR cascade (63). Several lines point to the localization of these particular pathways in the proximal tubule, among them the present TUNEL signal and related apoptotic cell features (23,61). With the UPR response also driving regulation of TFEB, an acknowledged master regulator of autophagy and lysosomal biogenesis (64), CsA may hereby induce a blockade in autophagic flux and cause the selective lysosomal disorder that was not observed in Tac. Notably, mTOR inhibitors, commonly employed in combination with CNI, may have a beneficial effect herein through their activation of TFEB (25,64,65). Stimulated *Arl8b* expression standing for enhanced lysosomal exocytosis, which we observed in the proximal tubule of the CsA group, supported the lysosomal issue (66). Upregulated HMGB1 and CTSD further suggested bioenergetic maladaption and mitochondrial dysfunction along with enhanced autophagy in CsA (60,67,68). The disorder may have been accompanied by oxidative stress since catalase was selectively stimulated in CsA along with activated proximal tubular peroxisomes, suggesting enhanced scavening of ROS (69). It is therefore reasonable to conclude that CsA-related cytotoxicity, among other sites, has a preferential site of action in this principal tissue component. Supportive evidence for a selective epithelial impact upon CsA further came from the comparison of our DEG signatures with published library data referring to the proximal tubule (Suppl. Fig. 15).

Unlike early data in rat focussing on PST as the primary target for CsA toxicity (59), the present changes typically began at the urinary pole and affected the entire length of PCT, but had little structural manifestation in PST; this discrepancy may be due to dose- and duration-related differences. Apoptosis in PCT was markedly higher in CsA than in Tac, but also included PST, suggesting damage potential in the S3 segments as well. Further advanced damage features indicated progression to similar loss of differentiation in either group, with

bioRxiv preprint doi: https://doi.org/10.1101/2023.04.05.535688; this version posted April 11, 2023. The copyright holder for this preprint (which was not certified by peer review) is the author/funder, who has granted bioRxiv a license to display the preprint in perpetuity. It is made available under aCC-BY-NC-ND 4.0 International license.

KIM-1 induction in BBM suggesting the promotion of mitochondrial fragmentation, production of ROS, cell cycle arrest, fibrosis and atrophy along with characteristic lipid accumulation (70).

Fibrotic foci in both CNI groups displayed an increased CD31-immunoreactive signal which was particularly enhanced in areas with sprouting-type capillaries; along with enhanced CD31 protein abundance in CNI, stimulated angiogenesis potentially counteracted endothelial toxicity of CNI (71). This result contradicted earlier findings on CsA effects in mice revealing diminished CD31 abundance (16); the difference may be species-related since mice develop milder CNI-NTX phenotypes and require high dosage levels. Diminished interstitial capillary fenestration, on the other hand, was generally comparable with the venous and glomerular endothelial pore reductions and not restricted to the fibrotic foci.

In view of earlier concepts emphasizing the role of distal segments in medulla and cortical medullary rays as the pathogenetic centerpieces in CNI nephropathy (29), our data could not confirm this pattern. TAL segments located in minor fibrotic foci showed little epithelial damage and likely reflected the loop of Henle-parts of proximally damaged nephrons; consequently, collapsed TAL lumina were rarely found.

In summary, results allowed us to identify potential mechanisms of CNI nephropathy under early chronic conditions. We have shown distinctive pathogenetic patterns arising in renal compartments under CsA vs. Tac medications. Besides common effects like fibrosis and atrophy, landmark differences were the predominant affections of the filtration barrier in Tac and of the PCT in CsA. Relevant protein signatures obtained from selective probing and multiomics analysis were ascribed to the respective renal microenvironments. These included disturbed VEGF/VEGFR2 signaling components preferentially in Tac as opposed to cytotoxic UPR signalling and altered autophagic flux in CsA. Products identified from multiomics were further characterized as differential pathognomonic biomarkers. The individual impact potential of these components has been been ranked and assigned in Fig. 12. Their multiplexed detection in patients may allow early diagnosis and prognosis to

bioRxiv preprint doi: https://doi.org/10.1101/2023.04.05.535688; this version posted April 11, 2023. The copyright holder for this preprint (which was not certified by peer review) is the author/funder, who has granted bioRxiv a license to display the preprint in perpetuity. It is made available under aCC-BY-NC-ND 4.0 International license.

prevent allograft failure. Data will also help to balance between both medications for long maintenance immunosuppression and design nephroprotective measures in order to minimize the side effects.

bioRxiv preprint doi: https://doi.org/10.1101/2023.04.05.535688; this version posted April 11, 2023. The copyright holder for this preprint (which was not certified by peer review) is the author/funder, who has granted bioRxiv a license to display the preprint in perpetuity. It is made available under aCC-BY-NC-ND 4.0 International license.

Materials and methods

Animals

Adult (10 to 12 week-old) male Wistar rats were divided into groups receiving CsA (Sandimmun, Novartis; target plasma trough level 3 µg/mL) and the respective vehicle (saline), or Tac (FK506, Selleckchem; target plasma trough level 3.5 ng/mL) and the respective vehicle (25% DMSO/75% PEG500, Sigma) via subcutaneously implanted osmotic minipumps (Alzet, 2ML4) for 28 days. For pump filling, 100 mg CsA and 7 mg Tac/mL of vehicle were used. For minipump implantation, rats were anesthetized by isoflurane inhalation. An incision of the neck skin was performed and the subcutaneous tissue dilated to create a pocket for the pump. The filled pump was then inserted into the pocket and the wound closed with metal clips. On the second last day of each experiment, rats were placed in metabolic cages for 24 h with water and chow ad libitum to collect urine. At the end of the experiments, rats were anesthetized with ketamin/xylavet (90/10 mg/kg BW; CP-Pharma) to obtain blood samples. Urine and blood samples were analyzed by a commercial laboratory (IMD Labor). For biochemical evaluation, one kidney was clamped and removed for biochemical analysis before perfusion fixation, or both kidneys were removed without fixation.

Blood and urine analysis

Blood was taken from the inferior vena cava using heparinized syringes, decanted into Eppendorf tubes, left for 30 min at room temperature (RT) for clotting, and centrifuged at 2.000xg for 10 min at 4 °C to obtain serum with the supernatant. Creatinine was measured and its clearance calculated using the formula, CrCl (mL/min) = (urine creatinine [mg/dL] × urine flow [mL/min] / serum creatinine [mg/dL]). Fractional excretion of sodium (FeNa) was calculated by the formula, FeNa (%)= (urinary sodium [mg/dL] × serum creatinine [mg/dL]) / (serum sodium [mg/dL] × urinary creatinine [mg/dL]).

Perfusion fixation and tissue processing

Kidneys were perfused via the abdominal aorta, first with 3% hydroxyethyl starch in 0.1 M Na-cacodylate (Caco) for 20 to 30 sec, then with 3% paraformaldehyde/3% hydroxyethyl

bioRxiv preprint doi: https://doi.org/10.1101/2023.04.05.535688; this version posted April 11, 2023. The copyright holder for this preprint (which was not certified by peer review) is the author/funder, who has granted bioRxiv a license to display the preprint in perpetuity. It is made available under aCC-BY-NC-ND 4.0 International license.

starch in Caco for 5 min. For paraffin embedding, tissue was post-fixed in the same fixation solution overnight at 4 °C, then transferred to Caco supplemented with 300 mOsm sucrose and 0.02% NaN3 until embedding. For cryostat sectioning, tissue was transferred directly after perfusion to 800 mOsm sucrose in Caco at 4 °C overnight, snap-frozen in 2-methyl butane cooled with liquid nitrogen, and stored at -80 °C. For histology and immunohistochemistry (IHC), tissues were dehydrated and paraffin-embedded. For electron microscopy, tissues were post-fixed overnight at room temperature in 1.5% glutaraldehyde/1.5% paraformaldehyde containing 0.05% picric acid in Caco, then in 1% osmium tetroxide/0.8% potassium hexacyanoferrate in Caco for 1.5 h at RT for TEM or in 1% aquaeous osmium tetroxide for SEM. Tissues were then dehydrated and embedded in epoxy resin for semithin sectioning and light microscopy (LM) or ultrathin sectioning and TEM analysis using standard methodology. For SEM, samples were high pressure-critical point-dried and sputter-coated.

Histology and immunostaining

For paraffin histology and IHC, 4 µm-thick sections were cut, mounted on glass slides, and deparaffinized. Histology was done using standard PAS, Masson's Trichrome, or Sirius Red staining protocols. For IHC, heat-induced epitope retrieval was generally performed for 6 min by cooking slides in citrate buffer (10 mM sodium citrate, pH 6.0) using a pressure cooker. Sections were blocked with 5% BSA (Serva) in TBS for 30 min at RT. Samples were then incubated overnight at 4 °C with primary antibody dissolved in 1% BSA/TBS or blocking medium (antibodies listed in Suppl. Table 1). After washing in TBS, fluorescently labeled secondary antibodies (Suppl. Table 1) were dissolved in 1% BSA/TBS or blocking buffer and incubated for 1 h at RT. Sections were then mounted in PBS-glycerol (1:9). Nuclei were stained with DAPI (Sigma). For immunoperoxidase staining, sections were incubated in methanol containing 0.3% hydrogen peroxide (H_2O_2) for 15 min, then in TBS, blocked at 37 °C for 30 min, washed, and incubated with primary antibody at 4 °C overnight, followed by HRP-conjugated secondary antibody diluted in 5% BSA/TBS for 1 h at RT. DAB (Sigma, D8001) containing 1% H_2O_2 was applied as a chromogen. Staining was monitored under LM;

bioRxiv preprint doi: https://doi.org/10.1101/2023.04.05.535688; this version posted April 11, 2023. The copyright holder for this preprint (which was not certified by peer review) is the author/funder, who has granted bioRxiv a license to display the preprint in perpetuity. It is made available under aCC-BY-NC-ND 4.0 International license.

reaction was stopped by washing with TBS. Samples were then dehydrated in a graded ethanol series, cleared with xylene, and mounted in Eukitt Quick-hardening mounting medium (Sigma).

Light microscopy and image processing

Images were acquired using a Zeiss LSM 5 Exciter confocal microscope (LSM) equipped with Imager.M1 and a NeoFluar objective lens (63x/NA 1.40). The laser lines used were 405, 488, 543, and 633 nm. Fluorescence images were acquired, some of them with additional differential interference contrast (DIC) overlay. The system was operated with Zen 2008 software (Zeiss). Immunoperoxidase, PAS, Masson´s trichrome, and Sirius red-stained sections were examined in bright-field microscopy under a Zeiss Axio Imager Z2 LM equipped with an ApoTome2 structured illumination acquisition system and a Plan-Apochromat 20x/0.8 objective using Zeiss ZEN 2012 software (blue edition). All image processing was done with ImageJ (NIH).

Filtration Slit Density Analysis

Kidney sections (2 µm) were deparaffinized and rehydrated, followed by boiling for 5 min in Tris-EDTA buffer (10 mmol/L Tris, 1 mmol/L EDTA, pH 9) in a pressure cooker for antigen retrieval. Next, sections were blocked in blocking solution (1% fetal bovine serum, 1% BSA, 0.1% fish gelatine, 1% normal goat serum) for 1 h. Primary antibodies (Suppl. Table 1) were incubated overnight at 4°C. After washing three times in PBS, secondary antibodies (Suppl. Table 1) were incubated for 1 h at RT. Nuclei were counterstained with DAPI for 5 min, followed by a washing step in PBS. Finally, the sections were washed in distilled H_2O and mounted in Mowiol 4-88 (Carl Roth) using high-precision cover glasses (Paul Marienfeld). The evaluation of the FSD was performed according to PEMP (72,73). 3D-SIM was performed with Z-stacks from 19 planes with 488 and 561 nm channels acquired from the stained kidney sections using an N-SIM super-resolution microscope (Nikon) equipped with a 100x silicone objective. The Z-stacks were converted into a maximum intensity projection followed by the automatized identification of the filtration slit length as an index of foot process effacement. FSD was expressed as the ratio of the total filtration slit diaphragm per

bioRxiv preprint doi: https://doi.org/10.1101/2023.04.05.535688; this version posted April 11, 2023. The copyright holder for this preprint (which was not certified by peer review) is the author/funder, who has granted bioRxiv a license to display the preprint in perpetuity. It is made available under aCC-BY-NC-ND 4.0 International license.

podocyte foot process area. FSD values of 20 glomeruli per animal were quantified in at least n=3 rats per group.

Electron microscopy

Samples from perfusion-fixed and post-fixed kidneys were embedded in Epon or transferred to critical-point drying for conventional TEM, large-scale scanning TEM (STEM), or SEM, respectively. Semithin sections (1 µm) were prepared from Epon blocks with an ultramicrotome (Ultracut E, Reichert-Jung) and stained with Richardson's stain for LM evaluation or to select a region for conventional or large-scale digitization. To screen pathological patterns ultrastructurally, conventional or large-scale ultrathin sections (200 to 400 nm) were prepared (74). Sections for large-scale analysis were partly or completely digitized at 3 to 4 nm pixel size using TrakEM2 for stitching and nip2 for export to high-resolution tif files and inspection with QuPath. Qualitative and quantitative analyses were performed using either a Gemini 300 field emission scanning electron microscope (FESEM, Zeiss) equipped with a scanning transmission electron microscopy (STEM) detector, SmartSEM, and Atlas 5 software. Alternatively, a Zeiss EM901 was used for conventional TEM. For repository implementation on www.nanotomy.org and open access pan-and-zoom analysis, datasets were exported into a tiled, browser-based file format using Atlas 5 software. For conventional 3D-SEM, dried and sputter-coated samples were evaluated by FESEM using an SEM detector.

Morphometric analysis

To assess tubulo-interstitial fibrosis from PAS-stained paraffin sections, brightness and contrast were adjusted in ImageJ. Lines were drawn around the perimeter of regions of interest (ROI); original magnification was 200x. Data were expressed as positively stained ROI vs. selected field areas. All samples were examined in a blinded manner. For quantitative assessment of α-SMA and renin immunoperoxidase staining, at least 15 non-overlapping fields were selected and α-SMA- and renin-immunoreactive ROI evaluated using ImageJ. The average ratio of ROIs to each microscopic field (200x magnification) was calculated and graphed. All measurements were performed by a single operator in a blinded

bioRxiv preprint doi: https://doi.org/10.1101/2023.04.05.535688; this version posted April 11, 2023. The copyright holder for this preprint (which was not certified by peer review) is the author/funder, who has granted bioRxiv a license to display the preprint in perpetuity. It is made available under aCC-BY-NC-ND 4.0 International license.

fashion. Estimation of glomerular podocytes was performed with WT1 and DAPI immunofluorescence staining using paraffin sections. Fluorescence signal was acquired on whole-slide images. Podocyte numbers per glomerulus were calculated from all glomeruli per section. To evaluate KIM-1 immunofluorescence signal, whole-slide images were acquired from anti-KIM-1-stained paraffin sections. The number of proximal tubular profiles carrying KIM-1 signal was counted in randomly selected fields. Endothelial pore density was determined by counting the number of fenestrae per micrometer of GBM in TEM images; total length of GBM was >750 µm per animal. At least 6 glomeruli per animal were evaluated. To determine fenestration density of cortical peritubular capillaries, TEM images were used. The number of fenestrae per micrometer of basement membrane length was counted. Ten cross-sectional profiles per animal were evaluated; total length of basement membrane was >850 µm per animal. Lysosome numbers in proximal tubules were counted on Richardson's stained semithin plastic sections. Conventional lysosomes were termed "dark" based on their dark-blue stained core; those with clear-appearing cores were termed "heterolysosomes". Twelve to 15 fields selected randomly, each containing 3 to 4 PCT profiles, were examined at 200x magnification. Wall-to-lumen ratios of renal afferent arterioles were analyzed in PAS-stained paraffin sections. Only profiles with open lumen were chosen. Wall and lumen surface areas were calculated using ImageJ by drawing lines around outer and inner perimeter. Five to 8 arterioles were studied per animal. The mean glomerular tuft area was measured by using anti-podocin-stained paraffin sections from entire kidneys imaged with the 3D-SIM. All available glomeruli with identifiable vascular pole were evaluated per section, their numbers ranging between 182 to 343. Podocin-immunoreactive area was quantified as μm^2 (NIPOKA). Quantification of anti-catalase immunofluorescence staining was performed by randomly selecting 10 optical fields, each containing 3 to 5 PCT profiles per slide at 200x magnification. Adjustments of pinhole, laser power, offset gain, and detector amplification below pixel saturation were maintained constant throughout. Mean fluorescence of catalase per PCT was determined with ImageJ. At least n=4 rats per group were evaluated throughout except for PAS-fibrosis and arteriolar morphometric measurements (n=3 rats).

bioRxiv preprint doi: https://doi.org/10.1101/2023.04.05.535688; this version posted April 11, 2023. The copyright holder for this preprint (which was not certified by peer review) is the author/funder, who has granted bioRxiv a license to display the preprint in perpetuity. It is made available under aCC-BY-NC-ND 4.0 International license.

TUNEL assay

Deparaffinized kidney sections (4 µm) were post-fixed in 4% PFA and labeled with TUNEL (Abcam, Ab66108) according to manufacturer's instructions in order to detect DNA fragmentation. Nuclei were counterstained with DAPI. Apoptotic signals were acquired by fluorescence microscopy (200x magnification) with DIC overlay. Labeled nuclei were counted in randomly chosen proximal tubular profiles from at least 10 adjacent optical fields and at least 15 randomly chosen glomeruli per animal, respectively. The apoptosis rate was calculated as the ratio of TUNEL-positive nuclei per total number of nuclei and field or glomerulus. At least n=4 rats per group were used for each experiment. Image analysis was performed with ImageJ.

Western Blotting

Whole kidney tissue was ground in liquid nitrogen and lysed in homogenization buffer (250 mM sucrose, 10 mM triethanolamine [AppliChem, PanReac, ITW Reagents]), supplemented with a protease inhibitor cocktail (cOmpleteTM, Roche), and sonicated 4 times for 1 s each. The supernatant of the protein lysates was obtained by centrifugation at 1.000xg for 10 min at +4 °C. Protein concentrations were measured using Micro BCA™ protein-assay-kit (Thermo Scientific). Samples were stored at -80 °C until further processing. Samples were then mixed 1:4 with 4x Laemmli buffer (Bio-Rad) containing 10% (v/v) β-mercaptoethanol (Merck), incubated at 65 °C for 10 min, separated by SDS PAGE (10% or 14%; 30 to 40 µg per lane), and transferred to a PVDF membrane (Macherey-Nagel). Membranes were then blocked with 5% milk or BSA in TBS and incubated with primary antibody overnight at +4 °C on a rotating wheel. Antibodies used for immunoblotting are listed in Suppl. Table 1. HRP-conjugated secondary antibody (Dako; diluted 1:2.000) was applied for 1 h at RT. Signal was generated by chemiluminescent reagent (Amersham ECL Western blotting detection reagent, GE Healthcare). Blots were imaged using an Intas ECL ChemoCam Imager (Intas Science Imaging). Densitometric quantification was performed using ImageJ.

RNA extraction and qualification

bioRxiv preprint doi: https://doi.org/10.1101/2023.04.05.535688; this version posted April 11, 2023. The copyright holder for this preprint (which was not certified by peer review) is the author/funder, who has granted bioRxiv a license to display the preprint in perpetuity. It is made available under aCC-BY-NC-ND 4.0 International license.

Whole kidney total RNA was isolated using PeqGOLD TriFast (VWR Life SCIENCE) according to manufacturer's instructions. The purity of RNA was checked using NanoPhotometer R spectrophotometer (IMPLEN). Next, an RNA Nano 6000 Assay Kit and Bioanalyzer 2100 system (Agilent Technologies) were used to evaluate quantity and integrity of RNA.

RNA sequencing and data processing

RNA-seq of rat kidney RNA samples (n=4 to 6 per group) was performed (Novogene, https://en.novogene.com/). A total amount of 1 µg RNA per sample was used as input material. Sequencing libraries were generated using NEBNext RNA Library Prep Kit for Illumina (New England BioLabs), and index codes were added to attribute sequences to each sample. Clustering of the index-coded samples was performed on a cBot Cluster Generation System with PE Cluster Kit cBot-HS (Illumina). After cluster generation, libraries were sequenced using Novaseq HisEquation 4000 platform (Illumina) and 150 bp paired-end reads were generated. Differential expression analysis between two groups was performed using DESeq2 R package. The resulting *P* values were adjusted using Benjamini and Hochberg's approach for controlling the False Discovery Rate (FDR). Genes with an adjusted *P* value < 0.1 (with no logFC cutoff) found by DESeq2 were considered as differentially expressed. RNA-seq data were deposited in the NCBI's Gene Expression Omnibus repository (GSE225215).

Global proteomics

Global proteomics was performed by using protein lysates of rat kidneys (n=4 to 6 per group) according to a previously established methodology (75) (Charité Core Facility for High Throughput Mass Spectrometry, Berlin). Briefly, protein lysates were trypsinized followed by analyzing tryptic peptides by LC-MS/MS using a timsTOF Pro 2 mass spectrometer (Bruker). The raw data were processed using DIA-NN 1.8 (76) with standard settings using MS1 and MS2 resolution of 10 ppm. Peptides were identified by library-free mode using the *Rattus norvegicus* UniProt (UniProt Consortium 2019) sequence database (UP000002494_10116, downloaded on 20210116) and the matched-between-runs (MBR) option. The output was

bioRxiv preprint doi: https://doi.org/10.1101/2023.04.05.535688; this version posted April 11, 2023. The copyright holder for this preprint (which was not certified by peer review) is the author/funder, who has granted bioRxiv a license to display the preprint in perpetuity. It is made available under aCC-BY-NC-ND 4.0 International license.

filtered at 0.01 FDR at the peptide level. All further analyses were performed using the R package DEP (77). Proteins with an adjusted *P* value < 0.1 (with no logFC cutoff) were considered as DEP. Data are deposited in the ProteomeXchange Consortium via the PRIDE partner repository with an accession number: PXD038841.

Global phosphoproteomics

Global phosphoproteomic analyses were perfomed (78) using cryo-pulverized rat kidney tissues (n=4 to 5 per group) (Proteomics/Max Delbrück Center, Berlin). Samples were lysed in SDC lysis buffer (1% Na-deoxycholate, 150 mM NaCl, 50 mM Tris-HCl pH 8.0, 1 mM EDTA, 10 mM DTT, 40 mM CAA [2-chloroacetamide, Sigma], phosphatase inhibitor cocktail II and III [Sigma]) by heating to 95 °C for 10 min. The solution was then cooled to RT, and Benzonase® (Merck; 50 units) was added for 30 min at 37 °C. Protein (200 µg per sample) was digested overnight at 37 °C with endopeptidase LysC (Wako) and sequence-grade trypsin (Promega) at a 1:100 enzyme-to-protein ratio. For relative quantification of phosphoproteins by liquid chromatography tandem mass spectrometry (LC-MS/MS), 200 µg per samples were labeled with TMTpro reagents (CsA sample set) or TMT10 (Tac sample set) according to manufacturer's protocols (Thermo Fisher Scientific). Isobarically-labeled peptides were combined and fractionated into 30 fractions using high pH-reversed phase chromatography. Samples of each fraction underwent phosphopeptide enrichment using immobilized metal affinity chromatography (IMAC). Flow-throughs after IMAC enrichment were collected and dried. Resulting powders were dissolved and separated in a high performance liquid chromatography system (Thermo Fisher Scientific). Samples were measured in a Q-Exactive HF-X instrument (Thermo Fisher Scientific) operated in data-adapted acquisition mode. Raw data were analyzed using v 1.6.10.44 MaxQuant software package (79). The internal Andromeda search engine was used to search MS2 spectra against a decoy rat UniProt database (release 2019-07) containing forward and reverse sequences. The FDR was set to 1% for peptide and protein identifications, respectively. Unique and razor peptides were included for quantification. Statistical analysis was done with the Perseus software (version 1.6.2.1). DEPP were calculated using Student´s *t*-test with

bioRxiv preprint doi: https://doi.org/10.1101/2023.04.05.535688; this version posted April 11, 2023. The copyright holder for this preprint (which was not certified by peer review) is the author/funder, who has granted bioRxiv a license to display the preprint in perpetuity. It is made available under aCC-BY-NC-ND 4.0 International license.

FDR based cutoff of 5%. The data presented in the study are deposited in the ProteomeXchange Consortium via the PRIDE partner repository, accession number PXD038546.

Gene ontology and pathway analyses

The Gene Ontology (GO) and pathway analyses for differentially expressed genes, proteins and phosphoproteins were performed using online bioinformatics tool Enrichr (https://maayanlab.cloud/Enrichr/). Pathways with a significance of $P < 0.05$ were defined as significantly regulated.

Statistics

Results were done in an observer-blinded way and analyzed using routine parametric statistics for normal distribution as assumed from the experimental design. Comparative analysis between two groups was performed by Student's *t*-test. Evaluation of multiple groups was performed using ANOVA followed by Tukey's post hoc test. GraphPad Prism7 software was used to analyze parameters. A significance level of $P < 0.05$ was accepted as significant.

Study approval

Animal experiments were approved by the German Animal Welfare Regulation Authorities for the protection of animals used for scientific purposes (Berlin Senate; G0148/18).

Author Contributions

SB and HD conceived and designed research; SB, HD, KM, and SP supervised animal experiments and tissue processing; HD, SB, SP, DEY, CD, and KM performed and analyzed histological, physiological, and biochemical experiments; HD, IAE, MM, CH, and SB designed and analyzed multiomic data; SB and HD designed figures; SB and HD drafted manuscript; SB, HD, CH, and KM approved final version of manuscript.

Acknowledgements

This work was financially supported by Deutsche Forschungsgemeinschaft BA700/22-2, MU2924/2-2, and SFB 1365-C04/-S01. HD was supported by a doctoral fellowship from Ministry of National Education, Turkey. We thank Hermann-Josef Gröne, Wilhelm Kriz,

bioRxiv preprint doi: https://doi.org/10.1101/2023.04.05.535688; this version posted April 11, 2023. The copyright holder for this preprint (which was not certified by peer review) is the author/funder, who has granted bioRxiv a license to display the preprint in perpetuity. It is made available under aCC-BY-NC-ND 4.0 International license.

Pontus Persson, David Ellison, and Richard Warth for constructive advice, Anette Drobbe for secretarial help, Kerstin Riskowsky, Katja Dörfel, Ariane Anger for expert technical help, Sara Timm, Petra Schrade, and John Horn (Core Facility for Electron Microscopy) for microscopical help, Junda Hu, Erdmann Seeliger, and Pontus Persson for physiological advice, Nicole and Tim Endlich (NIPOKA, Greifswald, Germany) for methodological help in 3D-SIM, and Lukasz Szyrwiel, Philipp Mertins, and Nils Blüthgen for bioinformatic data analysis.

Disclosures

The authors have declared that no conflict of interest exists.

bioRxiv preprint doi: https://doi.org/10.1101/2023.04.05.535688; this version posted April 11, 2023. The copyright holder for this preprint (which was not certified by peer review) is the author/funder, who has granted bioRxiv a license to display the preprint in perpetuity. It is made available under aCC-BY-NC-ND 4.0 International license.

References

1. Farouk SS, Rein JL. The Many Faces of Calcineurin Inhibitor Toxicity—What the FK? Adv Chronic Kidney Dis. 2020;27(1):56-66.

2. Naesens M, et al. Calcineurin Inhibitor Nephrotoxicity. Clin J Am Soc Nephrol. 2009;4(2):481-508.

3. Nankivell BJ, et al. Calcineurin Inhibitor Nephrotoxicity Through the Lens of Longitudinal Histology: Comparison of Cyclosporine and Tacrolimus Eras. Transplantation. 2016;100(8):1723-1731.

4. Kaufman DB, et al. Belatacept for Simultaneous Calcineurin Inhibitor and Chronic Corticosteroid Immunosuppression Avoidance: Two-Year Results of a Prospective, Randomized Multicenter Trial. Clin J Am Soc Nephrol. 2021;16(9):1387-1397.

5. Wissing KM, et al. Prospective randomized study of conversion from tacrolimus to cyclosporine A to improve glucose metabolism in patients with posttransplant diabetes mellitus after renal transplantation. Am J Transplant. 2018;18(7):1726-1734.

6. Leal R, et al. Pathology of Calcineurin and Mammalian Target of Rapamycin Inhibitors in Kidney Transplantation. Kidney Int Rep. 2018;3(2):281-290.

7. Liptak P, Ivanyi B. Primer: histopathology of calcineurin-inhibitor toxicity in renal allografts. Nat Rev Nephrol. 2006;2(7):398-404.

8. Mengel M, et al. Histological Characteristics of Calcineurin Inhibitor Toxicity—There Is No Such Thing as Specificity! Am J Transplant. 2011;11(12):2549-2550.

9. Bremer S, et al. NFAT-regulated cytokine gene expression during tacrolimus therapy early after renal transplantation: NFAT-regulated cytokine gene expression during tacrolimus therapy. Br J Clin Pharmacol. 2017;83(11):2494-2502.

10. Williams CR, Gooch JL. Calcineurin inhibitors and immunosuppression – a tale of two isoforms. Expert Rev Mol Med. 2012;14:e14.

11. Blankenstein KI, et al. Calcineurin inhibitor cyclosporine A activates renal Na-K-Cl cotransporters via local and systemic mechanisms. Am J Physiol Renal Physiol. 2017;312(3):F489-F501.

12. Cheriyan AM, et al. Calcineurin A-α suppression drives nuclear factor-κB-mediated NADPH oxidase-2 upregulation. Am J Physiol Renal Physiol. 2021;320(5):F789-F798.

13. Hoorn EJ, et al. Pathogenesis of calcineurin inhibitor–induced hypertension. J Nephrol. 2012;25(3):269-275.

14. Hu J, et al. Angiotensin II receptor blockade alleviates calcineurin inhibitor nephrotoxicity by restoring cyclooxygenase 2 expression in kidney cortex. Acta Physiol. 2021;232(1).

15. Kitamura M. Induction of the unfolded protein response by calcineurin inhibitors: a double-edged sword in renal transplantation. Nephrol Dial Transplant. 2010;25(1):6-9.

bioRxiv preprint doi: https://doi.org/10.1101/2023.04.05.535688; this version posted April 11, 2023. The copyright holder for this preprint (which was not certified by peer review) is the author/funder, who has granted bioRxiv a license to display the preprint in perpetuity. It is made available under aCC-BY-NC-ND 4.0 International license.

16. Labes R, et al. Daprodustat prevents cyclosporine-A–mediated anemia and peritubular capillary loss. Kidney Int. 2022;102(4):750-765.

17. Lazelle RA, et al. Renal Deletion of 12 kDa FK506-Binding Protein Attenuates Tacrolimus-Induced Hypertension. J Am Soc Nephrol. 2016;27(5):1456-1464.

18. Fedele AO, et al. Cyclosporin A but not FK506 activates the integrated stress response in human cells. J Biol Chem. 2020;295(44):15134-15143.

19. Krämer BK, et al. Efficacy and safety of tacrolimus compared with cyclosporin A microemulsion in renal transplantation: 2 year follow-up results. Nephrol Dial Transplant. 2005;20(5):968-973.

20. Lamoureux F, et al. Quantitative proteomic analysis of cyclosporine-induced toxicity in a human kidney cell line and comparison with tacrolimus. J Proteomics. 2011;75(2):677-694.

21. Cybulsky AV. Endoplasmic reticulum stress, the unfolded protein response and autophagy in kidney diseases. Nat Rev Nephrol. 2017;13(11):681-696.

22. Pallet N, et al. Cyclosporine-Induced Endoplasmic Reticulum Stress Triggers Tubular Phenotypic Changes and Death. Am J Transplant. 2008;8(11):2283-2296.

23. Yilmaz DE, et al. Immunosuppressive calcineurin inhibitor cyclosporine A induces proapoptotic endoplasmic reticulum stress in renal tubular cells. J Biol Chem. 2022;298(3):101589.

24. Klawitter J, et al. Low-Salt Diet and Cyclosporine Nephrotoxicity: Changes in Kidney Cell Metabolism. J Proteome Res. 2012;11(11):5135-5144.

25. Li Z, et al. Cyclosporine A blocks autophagic flux in tubular epithelial cells by impairing TFEB-mediated lysosomal function. J Cell Mol Med. 2021;25(12):5729-5743.

26. Andoh TF, et al. Comparison of acute rapamycin nephrotoxicity with cyclosporine and FK506. Kidney Int. 1996;50(4):1110-1117.

27. Klawitter J, et al. Association of Immunosuppressant-Induced Protein Changes in the Rat Kidney with Changes in Urine Metabolite Patterns: A Proteo-Metabonomic Study. J Proteome Res. 2010;9(2):865-875.

28. Lee JW, et al. Deep Sequencing in Microdissected Renal Tubules Identifies Nephron Segment–Specific Transcriptomes. J Am Soc Nephrol. 2015;26(11):2669-2677.

29. Stillman IE, et al. FK506 nephrotoxicity: morphologic and physiologic characterization of a rat model. Lab Invest. 1995;73(6):794-803.

30. Fasel J, et al. Light and Electron Microscopic Changes in the Kidney of Wistar Rats following Treatment with Cyclosporine A. Ultrastructural Pathol. 1987;11(4):435-448.

31. Wang X, et al. Tacrolimus Causes Hypertension by Increasing Vascular Contractility via RhoA (Ras Homolog Family Member A)/ROCK (Rho-Associated Protein Kinase) Pathway in Mice. Hypertension. 2022;79(10):2228-2238.

32. Hristovska AM, et al. Prostaglandin E 2 Induces Vascular Relaxation by E-Prostanoid 4 Receptor-Mediated Activation of Endothelial Nitric Oxide Synthase. Hypertension. 2007;50(3):525-530.

bioRxiv preprint doi: https://doi.org/10.1101/2023.04.05.535688; this version posted April 11, 2023. The copyright holder for this preprint (which was not certified by peer review) is the author/funder, who has granted bioRxiv a license to display the preprint in perpetuity. It is made available under aCC-BY-NC-ND 4.0 International license.

33. Purdy KE, Arendshorst WJ. EP 1 and EP 4 receptors mediate prostaglandin E 2 actions in the microcirculation of rat kidney. Am J Physiol Renal Physiol. 2000;279(4):F755-F764.

34. Rask-Madsen C, King GL. Differential Regulation of VEGF Signaling by PKC-α and PKC-ε in Endothelial Cells. Arterioscler Thromb Vasc Biol. 2008;28(5):919-924.

35. Sonveaux P, et al. Caveolin-1 Expression Is Critical for Vascular Endothelial Growth Factor–Induced Ischemic Hindlimb Collateralization and Nitric Oxide–Mediated Angiogenesis. Circ Res. 2004;95(2):154-161.

36. Baylis C. Nitric oxide deficiency in chronic kidney disease. Am J Physiol Renal Physiol. 2008;294(1):F1-F9.

37. Gallego MJ, et al. Cyclosporine enhances leukocyte adhesion to vascular endothelium under physiologic flow conditions. Am J Kidney Dis. 1996;28(1):23-31.

38. Markovic S, et al. In vitro effects of cyclosporin A on the expression of adhesion molecules on human umbilical vein endothelial cells. Clin Chim Acta. 2002;316(1-2):25-31.

39. Cheung K, et al. CD31 signals confer immune privilege to the vascular endothelium. Proc Natl Acad Sci USA. 2015;112(43).

40. Wang H, et al. Shear Stress Induces Endothelial Differentiation From a Murine Embryonic Mesenchymal Progenitor Cell Line. Arterioscler Thromb Vasc Biol. 2005;25(9):1817-1823.

41. Sluiter TJ, et al. Endothelial Barrier Function and Leukocyte Transmigration in Atherosclerosis. Biomedicines. 2021;9(4):328.

42. Hayashi A, et al. CD44 as a pathological marker for the early detection of calcineurin inhibitor-induced nephrotoxicity post kidney transplantation. Biomed Res. 2022;43(5):181-186.

43. Bernhardt A, et al. Inflammatory cell infiltration and resolution of kidney inflammation is orchestrated by the cold-shock protein Y-box binding protein-1. Kidney Int. 2017;92(5):1157-1177.

44. Kuppe C, et al. Common histological patterns in glomerular epithelial cells in secondary focal segmental glomerulosclerosis. Kidney Int. 2015;88(5):990-998.

45. Kim JH, et al. Influence of cyclosporine A on glomerular growth and the effect of mizoribine and losartan on cyclosporine nephrotoxicity in young rats. Sci Rep. 2016;6(1):22374.

46. Kobayashi M, et al. Glomerular endothelial changes in cyclosporine A-treated rats: Scanning and transmission electron microscopic studies. Jpn J Surg. 1991;21(2):210-215.

47. Xu C, et al. TNF-mediated damage to glomerular endothelium is an important determinant of acute kidney injury in sepsis. Kidney Int. 2014;85(1):72-81.

48. Nagao RJ, et al. Cyclosporine Induces Fenestra-Associated Injury in Human Renal Microvessels In Vitro. ACS Biomater Sci Eng. 2022;8(1):196-207.

bioRxiv preprint doi: https://doi.org/10.1101/2023.04.05.535688; this version posted April 11, 2023. The copyright holder for this preprint (which was not certified by peer review) is the author/funder, who has granted bioRxiv a license to display the preprint in perpetuity. It is made available under aCC-BY-NC-ND 4.0 International license.

49. Liu M, et al. Sox17 is required for endothelial regeneration following inflammation-induced vascular injury. Nat Commun. 2019;10(1):2126.

50. Tahir SA, et al. Caveolin-1 regulates VEGF-stimulated angiogenic activities in prostate cancer and endothelial cells. Cancer Biol Ther. 2009;8(23):2284-2294.

51. Satchell SC, Braet F. Glomerular endothelial cell fenestrations: an integral component of the glomerular filtration barrier. Am J Physiol Renal Physiol. 2009;296(5):F947-F956.

52. Wang Y, et al. Protein kinase D up-regulates transcription of VEGF receptor-2 in endothelial cells by suppressing nuclear localization of the transcription factor AP2β. J Biol Chem. 2019;294(43):15759-15767.

53. Guo JK, et al. WT1 is a key regulator of podocyte function: reduced expression levels cause crescentic glomerulonephritis and mesangial sclerosis. Hum Mol Genet. 2002;11(6):651-659.

54. Asfahani RI, et al. Activation of podocyte Notch mediates early Wt1 glomerulopathy. Kidney Int. 2018;93(4):903-920.

55. Moore CL, et al. TUNEL Assay: A Powerful Tool for Kidney Injury Evaluation. Int J Mol Sci. 2021;22(1):412.

56. Artelt N, et al. The Role of Palladin in Podocytes. J Am Soc Nephrol. 2018;29(6):1662-1678.

57. Menon R, et al. Glomerular endothelial cell-podocyte stresses and crosstalk in structurally normal kidney transplants. Kidney Int. 2022;101(4):779-792.

58. Tossidou I, et al. Tyrosine Phosphorylation of CD2AP Affects Stability of the Slit Diaphragm Complex. J Am Soc Nephrol. 2019;30(7):1220-1237.

59. Mihatsch MJ, et al. The side-effects of ciclosporine-A and tacrolimus. Clin Nephrol. 1998;49(6):356-363.

60. Zmijewska AA, et al. Bioenergetic maladaptation and release of HMGB1 in calcineurin inhibitor-mediated nephrotoxicity. Am J Transplant. 2021;21(9):2964-2977.

61. Han SW, et al. Prolonged Endoplasmic Reticulum Stress Induces Apoptotic Cell Death in an Experimental Model of Chronic Cyclosporine Nephropathy. Am J Nephrol. 2008;28(5):707-714.

62. Hetz C, Papa FR. The Unfolded Protein Response and Cell Fate Control. Mol Cell. 2018;69(2):169-181.

63. Higa A, et al. Endoplasmic Reticulum Stress-Activated Transcription Factor ATF6α Requires the Disulfide Isomerase PDIA5 To Modulate Chemoresistance. Mol Cell Biol. 2014;34(10):1839-1849.

64. Franco-Juárez B, et al. TFEB; Beyond Its Role as an Autophagy and Lysosomes Regulator. Cells. 2022;11(19):3153.

65. Silva Jr. HT, et al. Everolimus Plus Reduced-Exposure CsA versus Mycophenolic Acid Plus Standard-Exposure CsA in Renal-Transplant Recipients. Am J Transplant. 2010;10(6):1401-1413.

bioRxiv preprint doi: https://doi.org/10.1101/2023.04.05.535688; this version posted April 11, 2023. The copyright holder for this preprint (which was not certified by peer review) is the author/funder, who has granted bioRxiv a license to display the preprint in perpetuity. It is made available under aCC-BY-NC-ND 4.0 International license.

66. Wu PH, et al. Lysosomal trafficking mediated by Arl8b and BORC promotes invasion of cancer cells that survive radiation. Commun Biol. 2020;3(1):620.

67. Di YQ, et al. Autophagy triggers CTSD (cathepsin D) maturation and localization inside cells to promote apoptosis. Autophagy. 2021;17(5):1170-1192.

68. Tang D, et al. Endogenous HMGB1 regulates autophagy. J Cell Biol. 2010;190(5):881-892.

69. Godin N, Liu F, Lau GJ, et al. Catalase overexpression prevents hypertension and tubular apoptosis in angiotensinogen transgenic mice. Kidney Int. 2010;77(12):1086-1097.

70. Mori Y, et al. KIM-1 mediates fatty acid uptake by renal tubular cells to promote progressive diabetic kidney disease. Cell Metabol. 2021;33(5):1042-1061.e7.

71. Park S, et al. PECAM-1 regulates proangiogenic properties of endothelial cells through modulation of cell-cell and cell-matrix interactions. Am J Physiol Cell Physiol. 2010;299(6):C1468-C1484.

72. Siegerist F, et al. Structured illumination microscopy and automatized image processing as a rapid diagnostic tool for podocyte effacement. Sci Rep. 2017;7(1):11473.

73. Unnersjö-Jess D, et al. Three-Dimensional Super-Resolved Imaging of Paraffin-Embedded Kidney Samples. Kidney360. 2022;3(3):446-454.

74. Dittmayer C, et al. Preparation of Samples for Large-Scale Automated Electron Microscopy of Tissue and Cell Ultrastructure. Microsc Microanal. 2021;27(4):815-827.

75. Müller T, et al. Automated sample preparation with SP 3 for low-input clinical proteomics. Mol Syst Biol. 2020;16(1).

76. Demichev V, et al. DIA-NN: neural networks and interference correction enable deep proteome coverage in high throughput. Nat Methods. 2020;17(1):41-44.

77. Zhang X, et al. Proteome-wide identification of ubiquitin interactions using UbIA-MS. Nat Protoc. 2018;13(3):530-550.

78. Mertins P, et al. Proteogenomics connects somatic mutations to signalling in breast cancer. Nature. 2016;534(7605):55-62.

79. Tyanova S, et al. The MaxQuant computational platform for mass spectrometry-based shotgun proteomics. Nat Protoc. 2016;11(12):2301-2319.

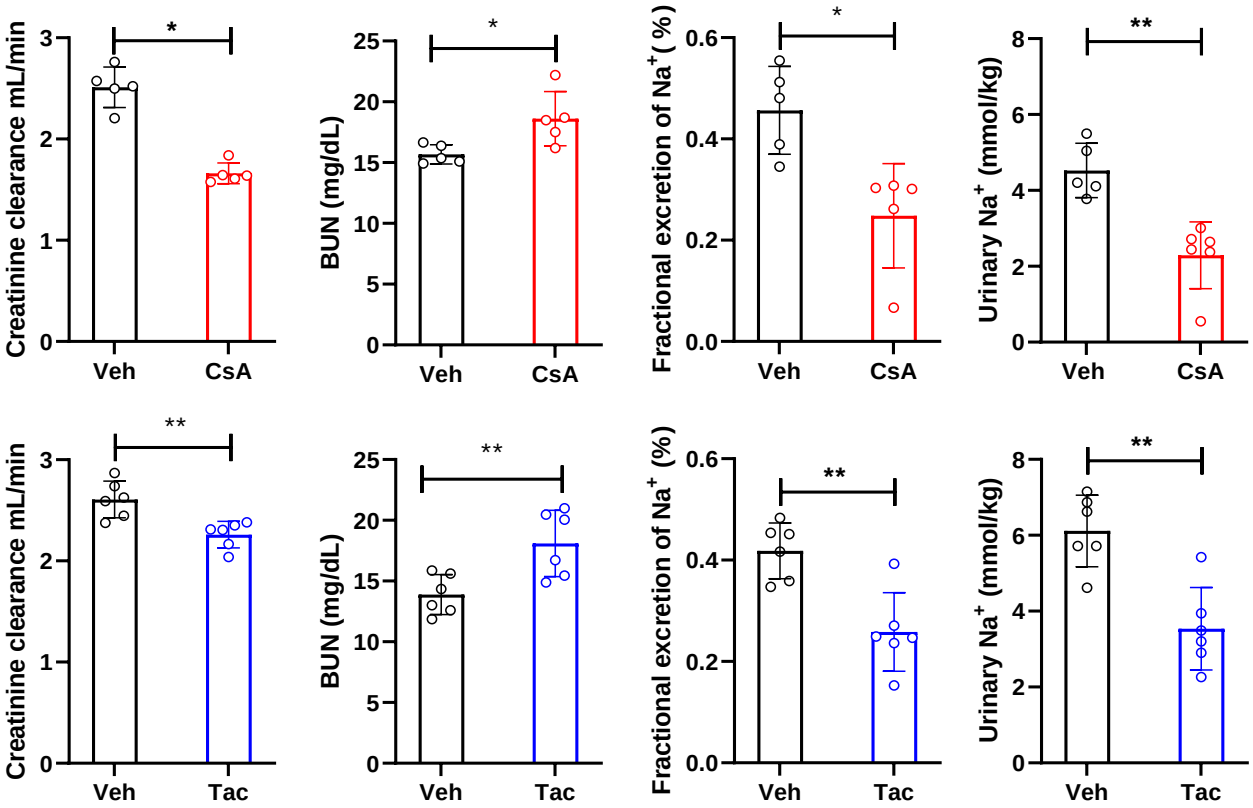

Figure 1. Physiologic parameters, graphs. Creatinine clearance, blood urea nitrogen (BUN), fractional sodium excretion, and urine sodium concentration were obtained from rats after 4 weeks of vehicle (Veh)-, cyclosporine A (CsA)- or tacrolimus (Tac)-treatment. Values, normalized for individual body weights, are means from n= 5 to 6 rats +/- standard deviation; * $P<0.05$, ** $P<0.01$. Statistical tests were performed using unpaired student's *t* test.

Table 1. Physiologic parameters, numerical values. Urine and blood parameters were obtained from rats after 4 weeks of treatment with vehicle (Veh), cyclosporine A (CsA), or tacrolimus (Tac). Values, normalized for individual body weights, are means +/- standard deviation; *P<0.05, **P<0.01,***P<0.001, ****P<0.0001. Statistical tests were performed using unpaired student's *t* test.

Parameter	Veh (n=5)	CsA (n=5)	*P value*	Veh (n=6)	Tac (n=6)	*P value*
Serum						
Na^+ [mmol/L]	139.34 ± 5.04	142.00 ± 0.71	0.31	143.6 ± 1.61	142.6 ± 1.42	0.282
Cl^- [mmol/L]	97.42 ± 2.57	91.74 ± 4.24	**0.039***	102.58 ± 0.70	100.68 ± 0.93	**0.002****
K^+ [mmol/L]	4.25 ± 0.77	4.50 ± 0.45	0.547	4.948 ± 0.80	4.703 ± 0.53	0.546
Ca^{+2} [mg/dL]	10.38 ± 0.84	9.67 ± 0.90	0.238	9.743 ± 0.40	10.118 ± 0.29	0.095
Phosphate [mg/dL]	8.09 ± 1.04	8.09 ± 0.49	0.994	9.063 ± 0.68	8.405 ± 0.54	0.094
Uric acid [mg/dL]	0.86 ± 0.85	0.92 ± 0.39	0.887	1.48 ± 0.97	1.13 ± 0.33	0.447
Lactate [mg/dL]	35.89 ± 18.34	37.53 ±12.87	0.874	34.16 ± 6.88	32.79 ± 4.81	0.697
Glucose [mg/dL]	146.77 ± 14.27	178.77 ± 3.02	**0.034***	150.6 ± 12.85	172.4 ± 10.29	**0.019***
Urea [mg/dL]	34.16 ± 2.79	39.84 ± 4.77	0.06	29.705 ± 3.53	8.72 ± 5.83	**0.011***
Creatinine [mg/dL]	0.306 ± 0.02	0.326 ± 0.02	0.216	0.288 ± 0.01	0.318 ± 0.01	**0.001*****
Cystatin C [mg/L]	0.40 ± 0.07	0.53 ± 0.04	**0.01****	0.38 ± 0.06	0.49 ± 0.07	**0.02***
Trough level [ng/mL]	0	3036.4 ± 125.6	**-**	0	3.42 ± 0.8	**-**

Parameter	Veh (n=5)	CsA (n=5)	*P value*	Veh (n=6)	Tac (n=6)	*P value*
Urine						
Na^+ [mmol/kg]	4.53 ± 0.72	2.29 ± 0.88	**0.001*****	6.11 ± 0.94	3.54 ± 1.08	**0.001*****
Cl^- [mmol/kg]	7.34 ± 0.81	6.86 ± 1.15	0.44	9.93 ± 1.03	12.14 ± 1.38	**0.01****
K^+ [mmol/kg]	10.19 ± 0.32	9.43 ± 0.91	0.1	12.04 ± 0.91	15.10 ± 1.34	**0.001*****
Phosphate [mg/kg]	8.76 ± 8.38	43.34 ± 8.87	**0.001*****	10.14 ± 4.74	59.96 ± 12.18	**0.0001******
Glucose [mg/kg]	11.14 ± 10.06	562 ± 588	0.07	19.68 ± 9.46	1204 ± 1444	0.1
Urea [mg/kg]	1469 ± 93	1382 ± 209	0.39	1809 ± 221	2309 ± 255	**0.005****
Creatinine [mg/kg]	24.05 ± 2.96	20.07 ± 1.90	**0.04***	30.07 ± 1.29	30.46 ± 1.71	0.67
Albumin [g/kg]	0.06 ± 0.03	0.14 ± 0.06	**0.02***	0.22 ± 0.03	0.19 ± 0.11	0.59
Urine flow [mL/24h]	23.0 ± 6.0	14.33 ±3.44	**0.03***	16 ± 3.03	21.33 ± 5.5	0.07
Osmolality [mOsm/kg]	1269 ± 364	1663 ± 268	0.08	1634 ± 209	1489 ± 214	0.3

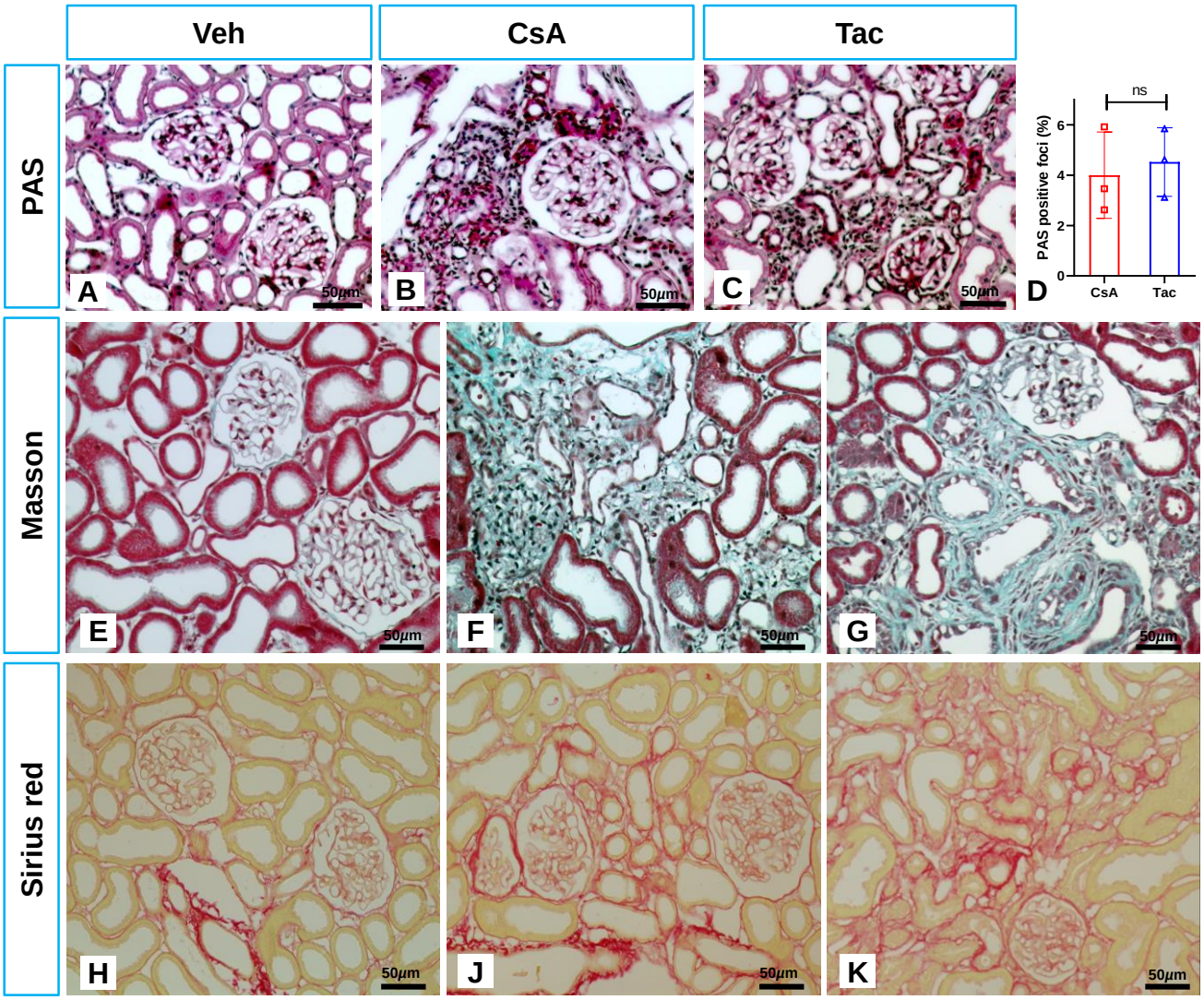

Figure 2. Histological overview. (A-C) Representative overviews of fibrotic foci in CsA and Tac; PAS. (D) Average size of PAS-stained fibrotic foci (percent of unit sectional area); values are means +/- SD; ns, not significant. (E-G) Green signal characterizes fibrotic foci in CsA and Tac. (H-K). Red staining indicates collagen deposits in fibrotic foci of CsA and Tac. Bars indicate magnification. Statistical tests were performed using unpaired student's *t* test (D).

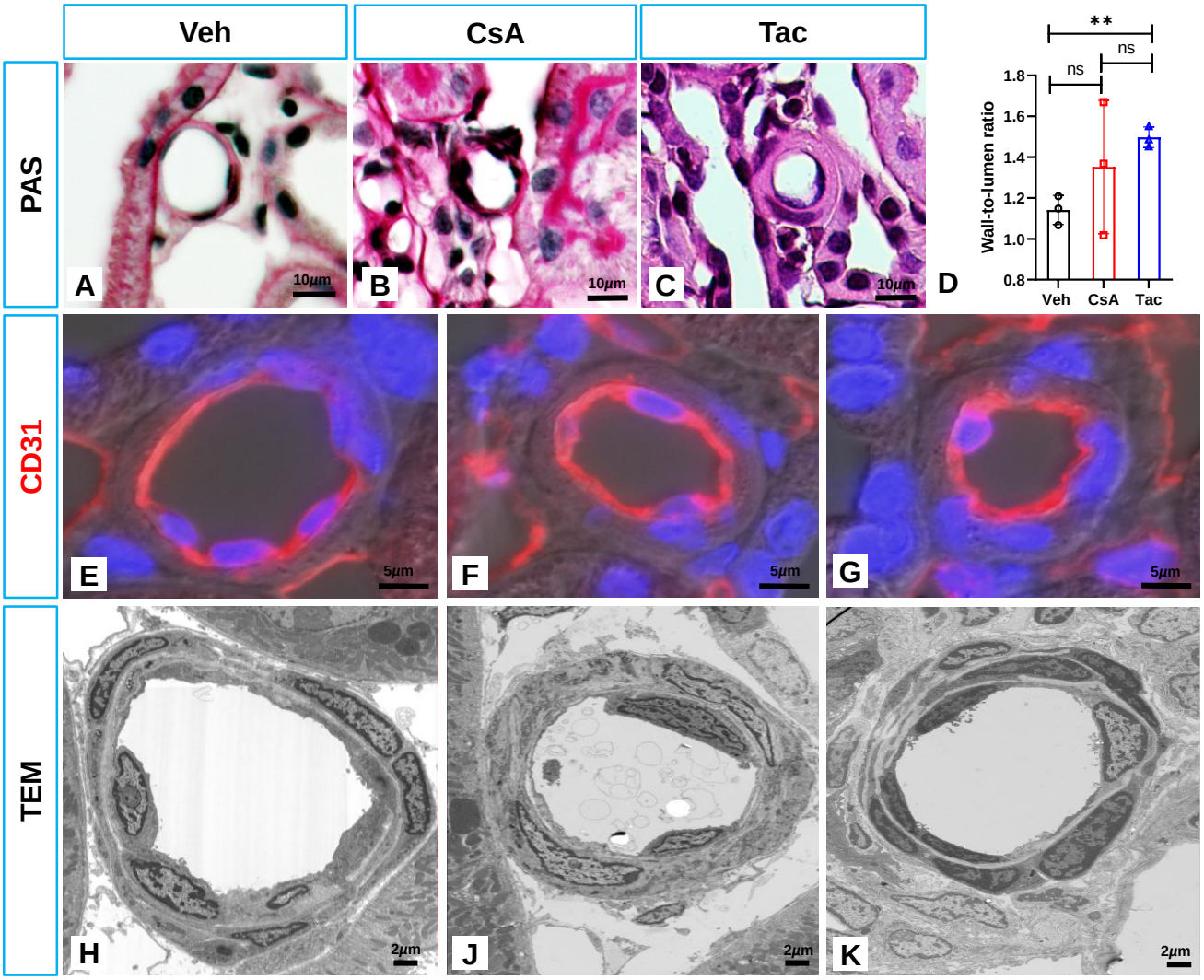

Figure 3. Renal afferent arteriolar structure. (A-C) Afferent arterioles, PAS. (D) Wall-to-lumen ratios; values are means +/- SD; ** *P*<0.01; ns, not significant (E-G) Wall structure and endothelial CD31 immunoreactivity. (H-K) Wall structure by TEM. DAPI blue nuclear staining and DIC optics (E-G); bars indicate magnification. Statistical tests were performed using ANOVA with Tukey's multiple comparison test (D).

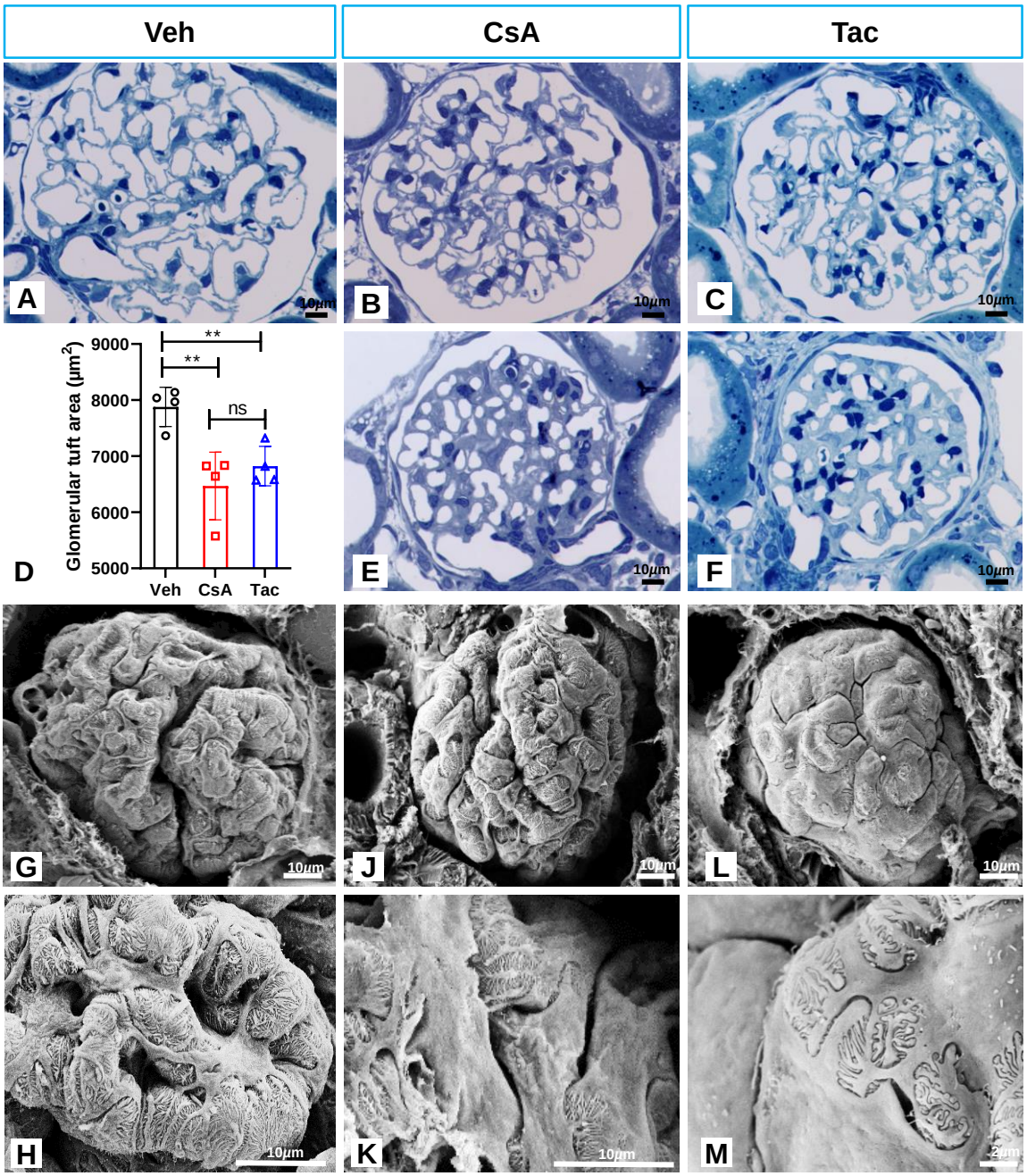

Figure 4. Glomerular structure. (A-C) Representative intact glomeruli, semithin sections, Richardson's stain. (D) Decreases in glomerular tuft size quantified from podocin-immunostained sections; means +/- SD; ** *P*<0.01; ns, not significant. (E,F) Glomeruli with tuft retraction, flattened podocytes, and narrowed capillaries. (G-M) Representative SEM of glomerular tufts as viewed from the urinary space after removal of Bowman's capsule. Note single capillaries with flattened podocytes and retracted or fused foot processes in CsA compared to generalized effacement of podocytes with broad cell bodies and rarified foot processes in Tac. Bars indicate magnification. Statistical tests were performed using ANOVA with Tukey's multiple comparison test (D).

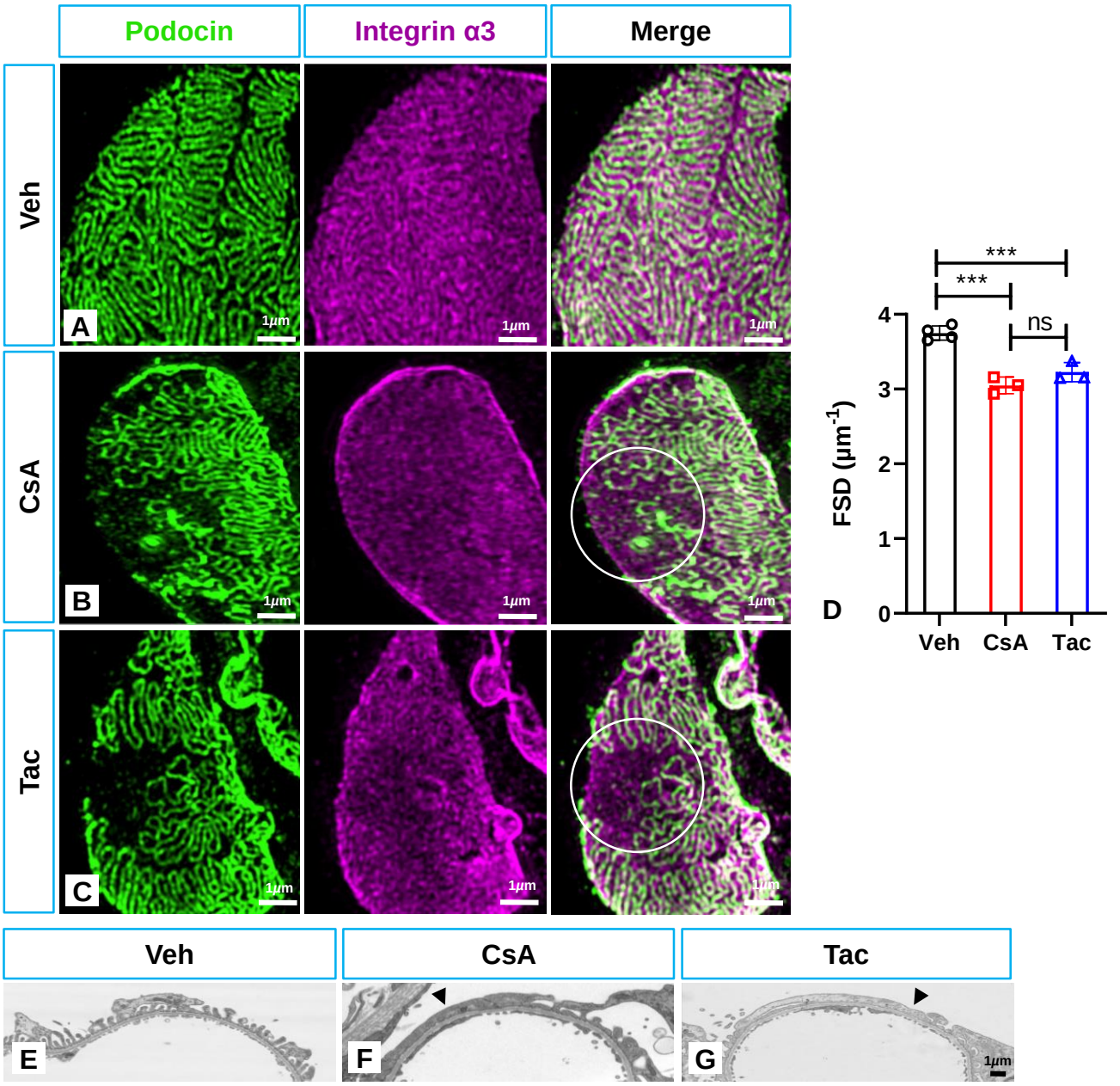

Figure 5. Glomerular capillaries – podocyte foot process effacement, changes in filtration slit density. (A-D) Double-immunostaining with anti-podocin antibody to label the filtration slit and anti-integrin α3 antibody to label the glomerular basement membrane. Filtration slit density (FSD) was determined by 3D-structured illumination microscopy (3D-SIM) and PEMP (72). Flat sections of capillary loops reveal sites of effacement in CsA and Tac (white circles in the merge images) by missing slit diaphragm of portions otherwise reactive for integrin α3 (B,C). Decreases in FSD in CsA and Tac; values are means +/- SD; *** $P<0.001$; ns, not significant (D). (E-G) Representative TEM images of the filtration barrier. Note foot process effacement in the CsA and Tac samples (arrowheads). Bars indicate magnification. Statistical tests were performed using ANOVA with Tukey's multiple comparison test (D).

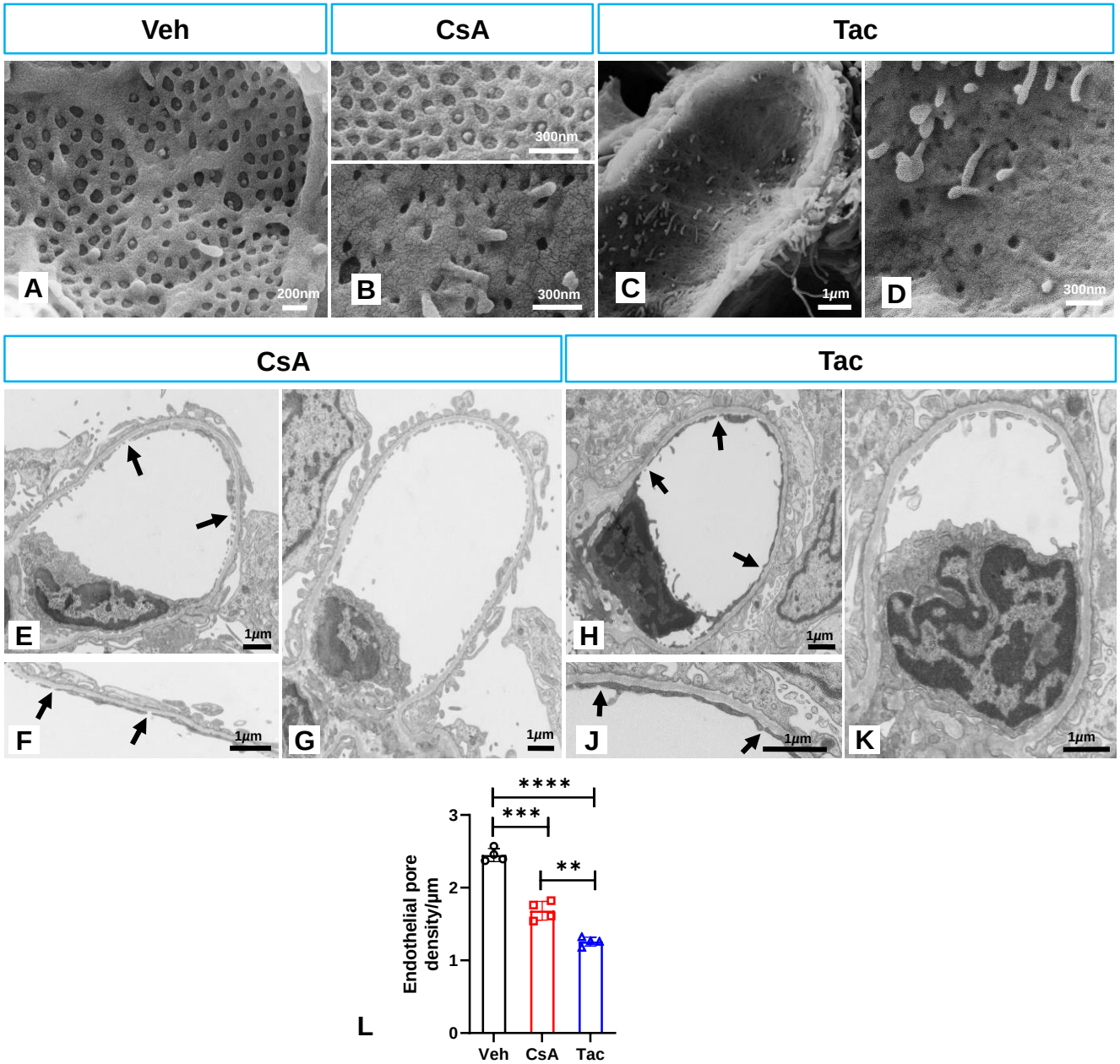

Figure 6. Glomerular capillaries - endothelial pore density. (A-D) Representative SEM images of glomerular capillary endothelial structure. Normal (top) or reduced pore density in CsA (below, B). Strongly diminished pore density in Tac (overview, C; detail, D). Note also smaller pore size in the CNI samples. (E-G) TEM showing characteristic capillary endothelial structure in CsA; capillaries with (between arrows; E,F) and without obvious pore losses (G). Detail in (F) is from another capillary. Note otherwise similar endothelial morphology in (E) and (G). (H-K) In Tac, capillaries with (between arrows; H,J) and without pore losses (K) detectable in parallel. Note striking condensation and darkening of endothelium when displaying pore losses (H). Bars indicate magnification. (L) Endothelial pore density per µm of GBM quantified from TEM sections; values are means +/- SD; ***P*<0.01, ****P*<0.001, *****P*<0.0001. Statistical tests were performed using ANOVA with Tukey's multiple comparison test (L).

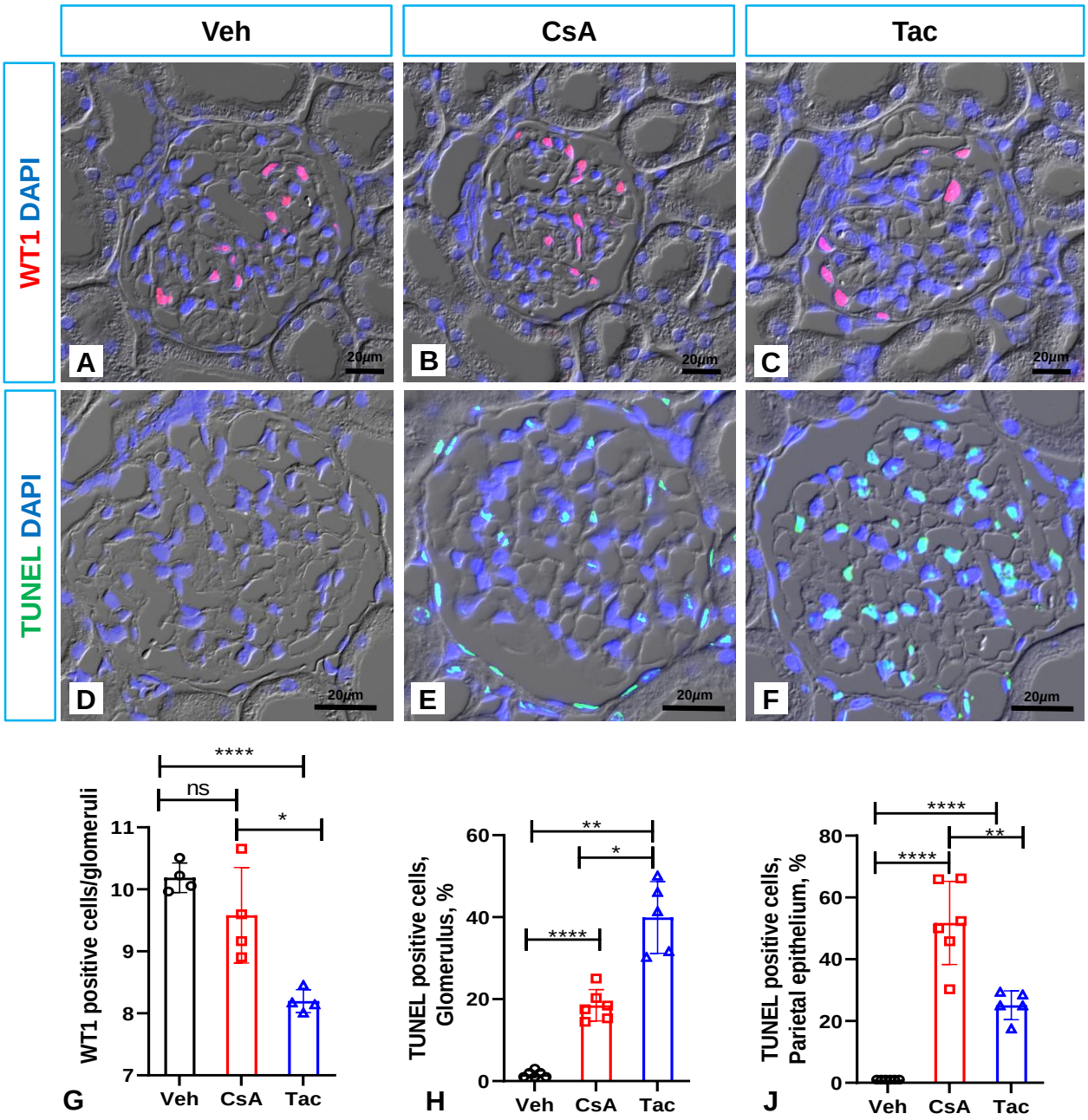

Figure 7. Glomerular WT1 expression and TUNEL labeling. (A-C) Anti-WT1 immunoreactivity in podocyte nuclei. (D-F) TUNEL immunofluorescence (light blue). Glomerular tuft and parietal epithelium show signals in CsA and Tac. DIC optics, DAPI nuclear stain (A-F); bars indicate magnification. (G-J) Quantification of signals; values are means +/- SD; *P<0.05; **P<0.01; ****P<0.0001; ns, not significant. Statistical tests were performed using ANOVA with Tukey's multiple comparison test (G-J).

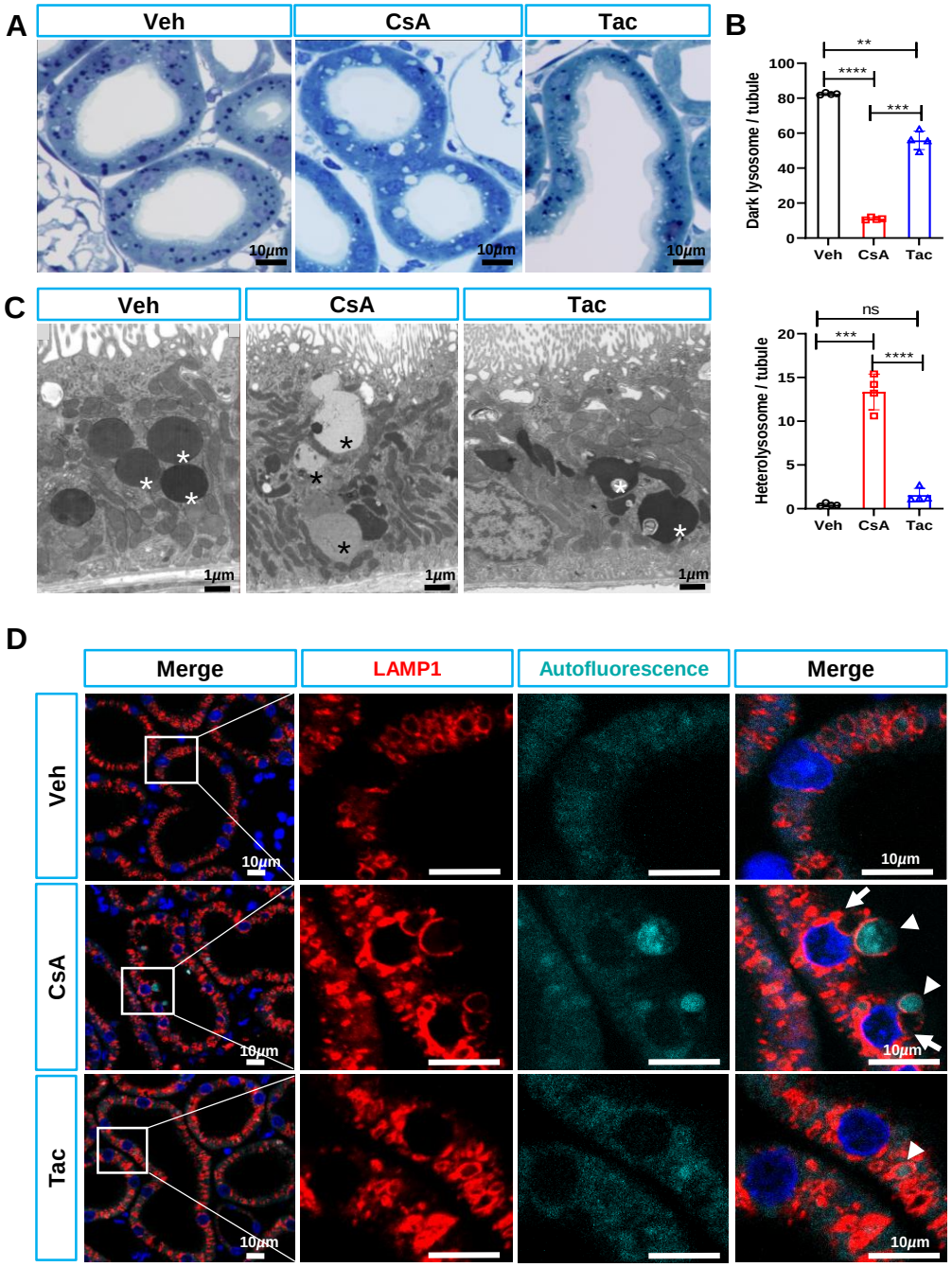

Figure 8. Lysosomal changes in proximal convoluted tubule. (A) Richardson‘s staining, semithin sections. Note large, clear heterolysosomes in CsA and diminished number of lysosomes in Tac. (B) Quantification of dark-stained lysosomes (top) and heterolysosomes (bottom); values are means +/- SD; ***P*<0.01;*** *P*<0.001; ****P*<0.0001; ns, not significant. (C) Lysosomal phenotypes by TEM. Note multiple heterolysosomes (asterisks) forming chains in apico-basal orientation in CsA; multiform lysosomes with heterogenous inclusions in Tac (asterisks). (D) Anti-LAMP1 immunofluorescence of lysosomal stages; boxes in overviews show details on the right; note large heterolysosomes with LAMP1-immunoreactive perimeters irrespective of autofluorescent (arrowheads) or non-autofluorescent content (arrows) in CsA; both selected heterolysosomes are in the process of luminal exocytosis. In Tac, large heterolysosomes and autofluorescent inclusions occur only rarely (arrowhead). DAPI nuclear stain. Bars indicate magnification. Statistical tests were performed using ANOVA with Tukey’s multiple comparison test (B).

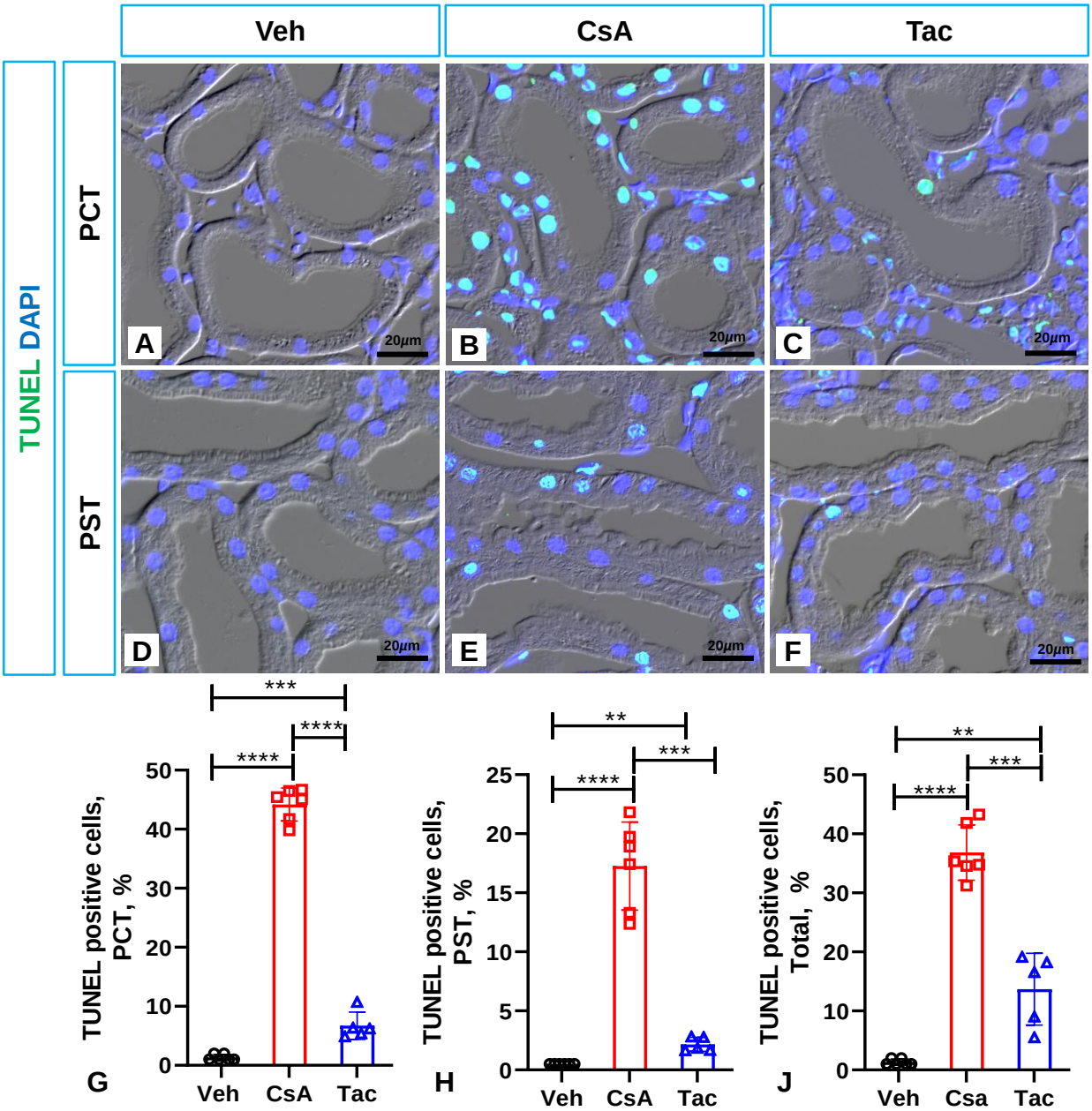

Figure 9. Proximal tubular TUNEL labeling. (A-F) TUNEL immunofluorescence; shows green nuclear signal in representative images. Note strong and frequent signal in CsA (B) and weak scattered signal in Tac PCT (C). Similar results in PST with less signal density in CsA (E). DIC optics, DAPI nuclear stain; bars indicate magnification. (G-J) Quantitative evaluation; total kidney TUNEL signal is shown for comparison (J). Percent of total nuclei counts; values are means +/- SD; ***P*<0.01***; *P*<0.001; *****P*<0.0001. Statistical tests were performed using ANOVA with Tukey's multiple comparison test (G-J).

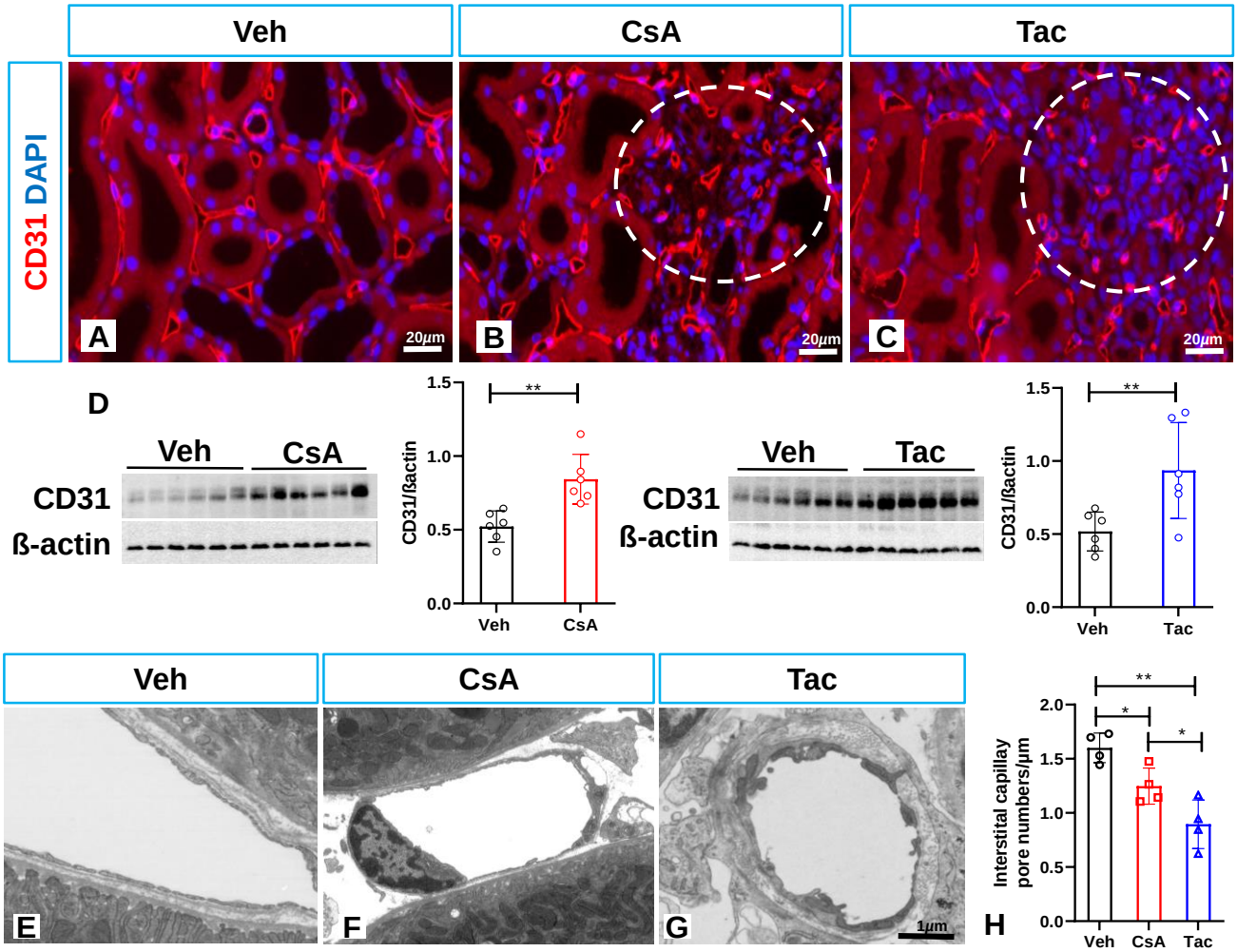

Figure 10. Changes in cortical interstitial vasculature. (A-C) Anti-CD31 immunofluorescence localized to peritubular capillaries. Note strongly positive capillaries of a rounded, sprouting type in fibrotic foci (encircled areas in B,C); DAPI nuclear blue staining. (D) Western blot CD31 signals (110 kDa) from kidney extracts of CsA, Tac and their respective Veh groups (n=6, respectively); ß-actin (42 kDa) serves as loading control. Densitometric evaluations on the right; data are means ± SD; ***P*<0.01. (E-G) TEM of cortical interstitial capillaries in fibrotic foci. Note sprouting type capillaries with absent fenestrae in CsA and Tac, and endothelial swelling or ridge formation particularly in Tac (G). (H) Endothelial pore density per µm of capillary basement membrane quantified from TEM sections; values are means +/- SD; * *P*<0.05, ** *P*<0.01. Bars indicate magnification. Statistical tests were performed using unpaired student's t test (D) or ANOVA with Tukey's multiple comparison test (H).

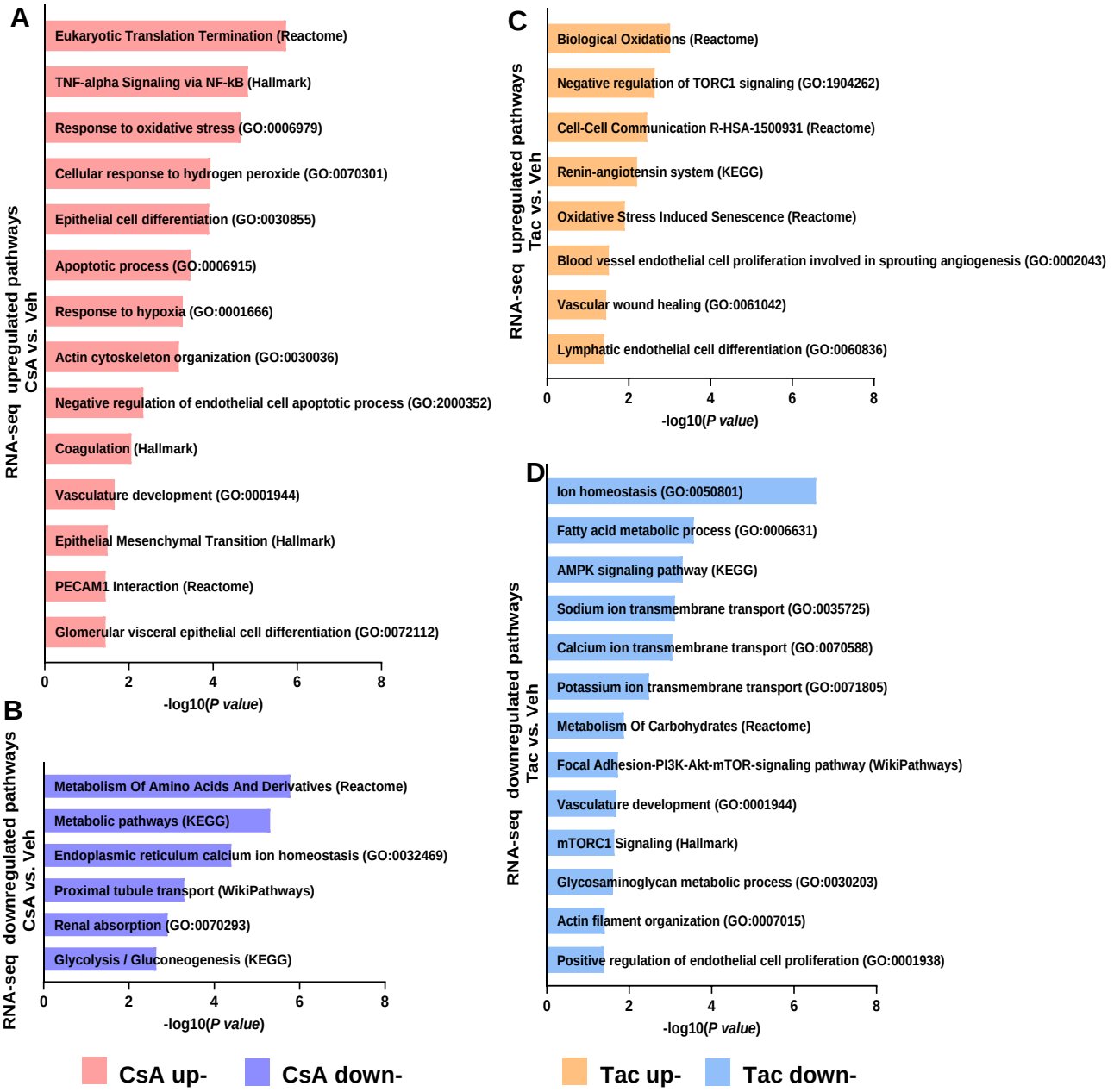

Figure 11. Pathway enrichment analysis of differentially expressed genes affected by CNI treatments. Treatment with CsA and Tac leads to different molecular pathway responses in chronic CNI nephrotoxicity. Significantly enriched pathways in genes upregulated (A) and downregulated (B) in CsA versus vehicles ($P < 0.05$). Significantly enriched pathways in genes upregulated (C) and downregulated (D) in Tac versus vehicles ($P < 0.05$). Term lists used in this analysis were GO_Biological_Processes, WikiPathways, Reactome, KEGG, and Hallmark to determine enriched processes and pathways from DEG (Enrichr webtool).

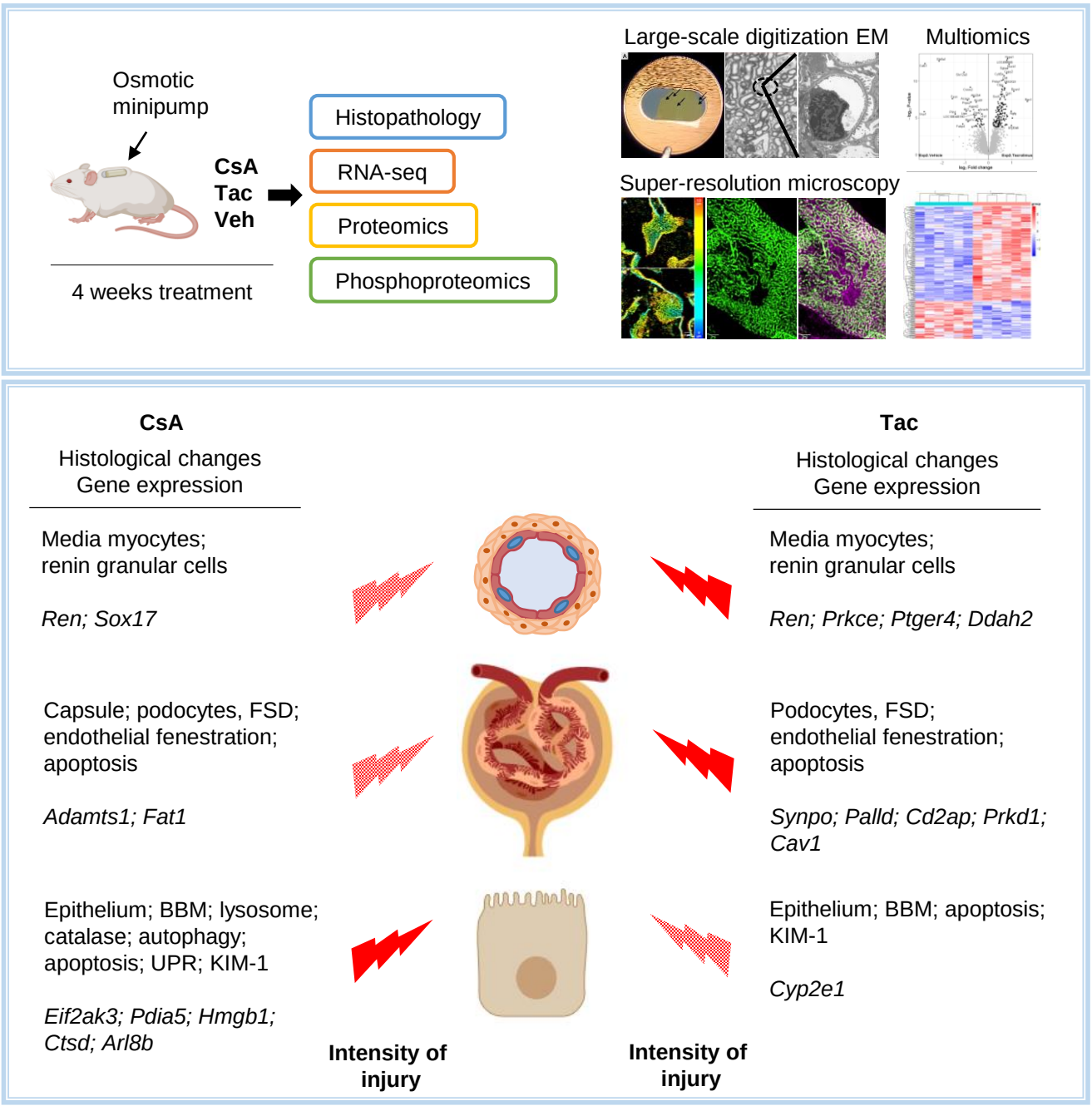

Figure 12. Main results of the study depicted as graphical abstract. Renal compartments and assigned gene expression, selected for their potential impact in CNI, are shown. Damage intensities are differentiated by rose (weaker) and red (stronger) arrows.